The Dissertation Committee for Chih-Hung Chen

certifies that this is the approved version of the following dissertation:

Scaling and instability of dynamic fracture

Committee:

Michael P. Marder, Supervisor

Harry L. Swinney

Richard Fitzpatrick

George T. Shubeita

Krishnaswamy Ravi-Chandar

Scaling and instability of dynamic fracture

by

Chih-Hung Chen, B.S.; M.S.

DISSERTATION

Presented to the Faculty of the Graduate School of

The University of Texas at Austin

in Partial Fulfillment

of the Requirements

for the Degree of

DOCTOR OF PHILOSOPHY

THE UNIVERSITY OF TEXAS AT AUSTIN

May 2014

Dedicated to my parents for their support and love.

Acknowledgments

First of all, I would like to express my sincere appreciation and gratitude to Dr. Michael Marder for his insightful guidance and endless support during my graduate studies at the University of Texas at Austin. I would like to thank Dr. Tadeusz Patzek for introducing me to the field of hydraulic fracturing and providing me with the opportunity to work in the Shell-UT Unconventional Research Program. I would like to acknowledge Dr. Harry Swinney and Dr. Bruce Rodenborn for providing me invaluable advice, support and training in the robot-swimmer experiments (PHY 380N research project). I would like to thank Dr. Krishnaswamy Ravi-Chandar, Dr. Johnathan Niemczura and Dr. Hepeng Zhang for their help and advice in the rubber experiments. All of the credit for chapter 2 is shared with them. I would like thank my dissertation committee members for the feedback, direction, and assistance.

I am grateful for all the help I have received from my colleagues and friends, including Anthony Bendinelli, David McGhan, Frank Male, Matt Guthrie, Maria Moura, Dhruv Bansal, Behzad Eftekhari, Saeid Enayatpour, and Andrea Keidel. Many thanks go to Olga Vera, Marybeth Casias, Rachael Salge and Sandy Taylor for always being so helpful, patient and friendly. This work can not be done without their help.

Finally, I would like to thank financial support from the United States

National Science Foundation, Condensed Matter and Materials Theory program and the Shell-UT Unconventional Research Program.

Scaling and instability of dynamic fracture

Chih-Hung Chen, Ph.D.
The University of Texas at Austin, 2014

Supervisor: Michael P. Marder

This dissertation presents three inter-related studies.

Chapter 2 presents a study of scaling of crack propagation in rubber sheets. Two different scaling laws for supersonic and subsonic cracks were discovered. Experiments and numerical simulations have been conducted to investigate subsonic and supersonic cracks. The experiments are performed at 85 °C to suppress strain-induced crystallites that complicate experiments at lower temperature. Calibration experiments were performed to obtain the parameters needed to compare with a theory including viscous dissipation. Both experiments and numerical simulations support supersonic cracks, and a transition from subsonic to supersonic is discovered in the plot of experimental crack speed curves versus extension ratio for different sized samples. Both experiments and simulations show two different scaling regimes: the speed of subsonic cracks scales with the elastic energy density while the speed of supersonic cracks scales with the extension ratio. Crack openings have qualitatively different shapes in the two scaling regimes.

Chapter 3 describes a theory of oscillating cracks. Oscillating cracks are not seen very widely, but observed in rubber and gels. A theory has been proposed for the onset of oscillation in gels, but the oscillation of cracks in rubber has not been explained. This study provides a theory able to describe both rubber and gels and recover the experimental phase diagram for oscillating cracks in rubber. The main new idea is that the oscillations of cracks follow from basic features of fracture mechanics and are independent of details of the crack equation of motion. From the fact that oscillations exist, one can deduce some conditions on forms that equations of motion can take.

A discrete model of hydraulic fracture is mentioned in Chapter 4. Hydraulic fracturing is a stimulation treatment wherein fluids are injected into reservoirs under high pressure to generate fractures in reservoirs. In this study, a lattice-based pseduo-3D model is developed to simulate hydraulic fracturing. This mode has been validated via a comparison with the KGD model. A series of pilot simulations was systematically tested for complex geometries under more realistic operation conditions, including flexible boundary conditions, randomness in elastic properties of shales and perforations. The simulation results confirm that perforation is likely to increase the complexity of fracture networks; the results also suggest that the interference between neighboring fractures is key to fracture network formation.

Table of Contents

List of Figures

Chapter 1

Introduction

The modern theory of fracture, called linear elastic fracture mechanics, was originated by A. A. Griffith in the 1920s based on his observations of fractures in glass [26] and extended by Irwin [30] and Orowan [51]. Linear elastic fracture mechanics provides fundamental understanding of fracture processes and enables us to characterize these processes by using a set of useful parameters, which includes fracture toughness, stress intensity factors, strain energy release rate, etc. Today, these fracture mechanics parameters are widely used in applied mechanics and material engineering communities. Nevertheless, linear elastic fracture mechanics still fails to provide satisfactory answers to these following essential questions: (1) how fast can cracks propagate in brittle materials? (2) how does a crack choose its direction? and (3) can we understand complex fractures and even manipulate them?

This research contains three inter-related studies that are inspired by these open questions. Results from this research are expected to improve our understandings of dynamic cracks. This introductory chapter presents an overview of this research and background information on the numerical

methodology used in this research.

1.1 Projects overview

Chapter 2 presents a study motivated by a fundamental question in fracture mechanics: "How fast can cracks propagate in brittle materials?" A single crack can accelerate by consuming the elastic energy stored in a solid medium. It was long believed that cracks cannot propagate faster than sound speeds [18, 55]. In brittle plastics or brittle crystals, once a crack moving faster than a critical speed, on the order of half of Rayleigh wave speed, crack tip loses its stability and sprouts microscopic branches [15, 16, 54]. However, cracks in natural rubber are different. Natural rubber can prevent the micro-branching instability spontaneously and allows cracks to propagate faster than the speed of sound [53]. Based on a supersonic rupture theory proposed for the supersonic cracks in rubber, there exist two different scaling regimes for the crack speed: speeds of supersonic cracks should be independent of system size if strain is held constant, in contrast to subsonic cracks whose speed is independent of system size if energy density is held constant [40].

However, at room temperature and large strains, natural rubber undergoes strain-induced crystallization, which greatly complicates the velocity response of cracks [63]. A previous study suggests that this undesirable toughening effect can be reduced by raising the temperature to 85 °C [63]. Based on this reason, experiments in this study are designed to be conducted at 85

°C where the strain crystallization is suppressed. This study also develops a numerical model of rubber fracture with a minimal number of adjustable parameters used to compare with the experiments. The significant contribution of this study is to provide the first confirmation of the supersonic rupture theory.

Chapter 3 describes a theoretical study of oscillatory instability in fast cracks. The fundamental theory of fracture mechanics provides good understandings of cracks moving in a straight line. However cracks can create much more complicated geometrical patterns, such as branched structures and oscillations. Oscillating cracks are rarely seen, but they were observed in rubber [13] and in gels [35]. Bouchbinder et al. [3] provided a theory for the onset of oscillation in gels, but this theory cannot explain the main experimental findings in rubber, which include a phase diagram for oscillations as a function of biaxial loading, and measurements of amplitude and wavelength of oscillation once the wiggling begins.

Although the equation of motion for cracks in rubber is not known, the experimental results suggest that the phase diagram of oscillating cracks in rubber requires almost no knowledge of the equation of motion altogether. Inspired by this suggestion, the main idea of this study is that the oscillations of cracks follow from basic features of fracture mechanics and are independent of details of the crack equation of motion. The goal of this study is to provide a theory based from this idea, which is able to describe both rubber and gels and recover the experimental phase diagram for oscillating cracks in rubber.

Chapter 4 presents a numerical study in a project named "Physics of Hydrocarbon Recovery in Shales," which is one of the programs in the Shell-UT Unconventional Research Program. This project began in February 2012 and is ongoing.

Hydraulic fracturing is a standard well stimulation treatment that enhances the production of oil or gas originally locked in low permeability reservoirs. This is not a brand new technology; the very first application of this technology was used to produce oil and gas in Kansas's Hugoton field in 1947 [1, 23]. Since then, hydraulic fracturing has been used in more than one million oil and gas wells [28].

The development of simple theoretical models of hydraulic fracturing started in the 1950s. Two classical simplified models, the PKN model and the KGD model, provide relatively simple analytical solutions for single planar pressure-driven fracture problems [20, 33, 48, 52]. However, more and more evidence shows that the pattern of hydraulic fractures can be complex [12, 17, 21, 50].

Characterizing the connectivity of these complex fracture networks is a key factor in predicting well performance, but, unfortunately, the existing single-planar-fracture models are not able to model these complex fracture networks. Therefore, the primary goal of this study is to develop a discrete model that can simulate complex fracture networks under various operation conditions and a qualitative study of these patterns will follow.

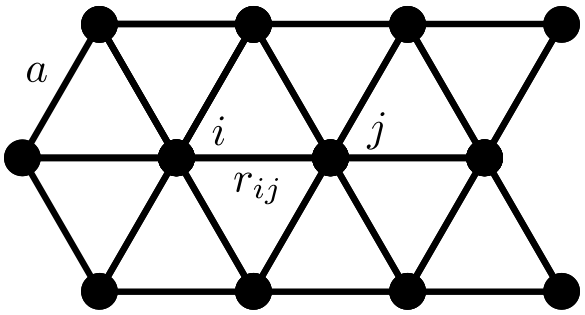

Figure 1.1: A triangular lattice of lattice spacing a. The distance between two neighbor nodes i and j is denoted by r_{ij}. The elastic interaction between i and j vanishes once r_{ij} is greater than its elastic limit r_c.

In sum, the current theory of fracture provides very limited understanding of dynamic cracks. These three studies as a whole try to find satisfactory explanations for supersonic cracks in rubber, oscillating cracks in rubber and gels, and complex hydraulic fracture networks. The results of this research are expected to provide some insights into complex fracture dynamics.

1.2 Numerical methodology

The numerical approach used in this research is originated from Slepyan's lattice models for dynamic cracks [59]. This discrete mass system can accommodate complex fracture geometries at mesoscopic and microscopic scales. A number of studies based on lattice models have been done before, for example, complete analytical solutions for dynamic fracture problems at the atomic scale [38, 41], and a numerical method for the rupture of rubber [39, 40] that eventually led to detailed comparison with experiment [9, 63].

In this model, there is a set of mass points arranged on a triangle lattice with a lattice spacing a, and the spring between two mass points represents their elastic interactions, as shown in fig. 1.1. The spring snaps once its length is greater than its elastic limit, r_c. This limit might be just a constant, or it might depend on many factors, such as local deformations. In general, a triangular lattice is just a convenient choice for modeling isotropic medium, and there are many other lattice choices, such as square lattice and hexagonal lattice. Lattice choices may depend on macroscopic properties of materials and details of system.

An equation of motion for this setup can be obtained by the following considerations. Let U describe the strain energy functional of this system and let $\vec{r_i}$ describe the position of mass point i. The conservative force on mass point i is $f^\alpha = -\partial U/\partial u_i^\alpha$, where α ranges over x, y and z. Let $\vec{g}$ represent the dissipative force, and then the equation of motion reads

$$m\frac{\partial^2 \vec{r_i}}{\partial t^2} = \sum_{j\in n(i)} \left(\vec{f} + \vec{g}\right) \theta\left(r_c - r_{ij}\right), \tag{1.1}$$

where $r_{ij} = |\vec{r_j} - \vec{r_i}|$, j is one of the nearest neighbors of i, m is the mass in a unit cell and θ is the Heaviside step function. Both $\vec{f}$ and $\vec{g}$ will become zero once the elongation of the spring r is greater than r_c. In this research, the dissipative force is chosen to be Kelvin dissipation where $\vec{g}$ proportional to the relative velocities of two particles, i.e., $\vec{g} = \beta\left(\vec{v_j} - \vec{v_i}\right)$. This proportional constant β can be measured from calibration experiments.

Chapter 2

Scaling of Crack Propagation in Rubber Sheets

This chapter presents the study in supersonic cracks and subsonic cracks in rubber sheets; all the results have been published in EPL [9]. All of the credit for this work is shared with Dr. Hepeng Zhang, Dr. Johnathan Niemczura, Dr. Krishnaswamy Ravi-Chandar and Dr. Michael Marder.

2.1 Introduction

The motivation of this project is to investigate a fundamental question in fracture mechanics: "How fast can cracks propagate in brittle materials?" It was long believed that a crack cannot propagate faster than sound speeds [18, 55]. A single crack in a brittle material can accelerate by consuming elastic energy stored when material is stretched. But there seems to be a limiting speed for crack motion. Transport of stored energy to the crack tip is described by an energy flux tensor, and once the crack speed exceeds a critical value — the Rayleigh wave speed — the integrated energy flux becomes imaginary or

negative. Thus one reaches the conventional conclusion that "the *limiting crack speed* in modes I and II is the Rayleigh wave speed and in mode III, the shear wave speed."([55], p. 73). In materials such as brittle plastics or brittle crystals, cracks do not even reach the Rayleigh wave speed. Instead, crack tips become unstable and sprout complicated three-dimensional branches when cracks pass a lower critical speed, on the order of half of Rayleigh wave speed [15, 16, 54].

However, cracks in rubber are different. Natural rubber can prevent the micro-branching instability spontaneously and allows cracks to propagate faster than the speed of sound [53]. According to a supersonic rupture theory developed to explain the observations, velocities of supersonic cracks should be independent of system size if strain is held constant, in contrast to subsonic cracks whose velocity is independent of system size if energy density is held constant [40]. Nevertheless it has not been possible to compare theory and experiment in detail. At room temperature and large strains, natural rubber undergoes an increase in toughness of several orders of magnitude due to strain crystallization, greatly complicating the velocity response of cracks [63].

In this chapter, experiments are conducted at 85 °C where the strain crystallization is suppressed. A satisfactory quantitative description of the supersonic cracks is obtained, and the results show that both subsonic and supersonic propagation obey the predicted scaling laws.

2.2 Experimental methods

The experiments were designed and performed by Hepeng Zhang, a former postdoc researcher in our group, and Johnathan Niemczura, a former graduate student in the Department of Aerospace Engineering and Engineering Mechanics.

The purpose of this study is to understand the relation between crack speed and extension ratio in rubber sheets for opening mode cracks. The sheets are 0.15 mm thick with mass density ρ is 930 kg/m^3. Extension ratio is defined as the ratio of the length of stretched specimens to the original length. In the experiments, natural rubber sheets are stretched uni-axially over a range of extension states: the extension ratio in the crack propagation (x) direction is constrained to be $\lambda_x = 1$ while the extension ratio λ_y along the loading (y) direction is varied between 1 and 5. The extension ratio in the thickness (z) direction is $\lambda_z = 1/(\lambda_x\lambda_y) = 1/\lambda_y$ because natural rubber is highly incompressible.

After rubber is stretched to a desired extension level, the sheet is clamped between a pair of rectangular steel frames. All frames have the same length 66 cm in the x direction and different heights in the y direction (h=5.1, 10.2, and 17.8 cm) as shown in fig. 2.1. A 1 mm long initial cut inserted into the prestretched sheet with a blade can result in either dynamic fracture propagation or a stationary fracture opening depending strongly on the stretched state [34, 53, 63]. Once the crack begins propagating, it reaches a steady state, typically within less than 0.05 s. The fracture resistance determines crack

speeds and it is greatly enhanced by strains at room temperature. X-ray diffraction measurements of scattering intensity from the crystalline phase of rubber and systematic measurements of crack motion in rubber sheets, show that strain-induced crystallization occurs at 24 °C when the extension ratio $\lambda_y > 3$. This toughening effect can be reduced by raising the temperature. Previous studies show that crack speeds increase monotonically with λ_y up to $\lambda_y = 5$ at 85 °C [63]. All experiments mentioned in this chapter were performed at 85 °C for extension ratios $\lambda_y < 5$ so that crystallization should not be important.

Crack motion was recorded with video at 48000 frames per second at a resolution of 384×256 pixels. By decorating the rubber sheet with ink marks and comparing consecutive frames particle velocities could be extracted in the rubber sheet, as well as the velocity of the crack. Some results appear in fig. 2.5.

2.3 Numerical Model

A computational model of rubber fracture with a minimal number of adjustable parameters was developed and used to compare with the experiments. At the continuum level, let's express deformations in terms of finite strain tensor

$$E_{\alpha\beta} = \frac{1}{2}\left(\sum_{\gamma} \frac{\partial u_\gamma}{\partial r_\alpha}\frac{\partial u_\gamma}{\partial r_\beta} - \delta_{\alpha\beta}\right). \tag{2.1}$$

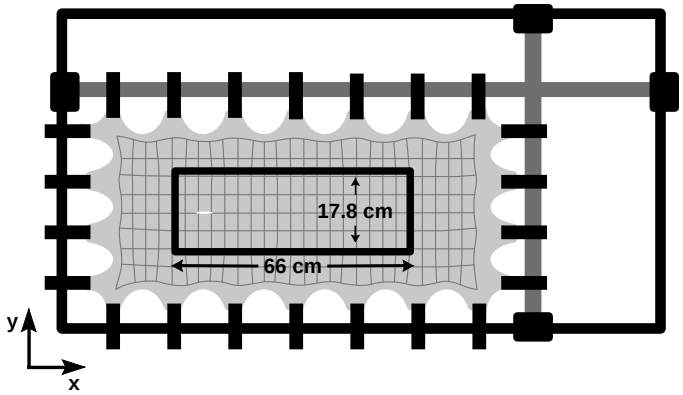

Figure 2.1: Experimental setup for stretching rubber sheets in the vertical (y) direction. After the sheet has been extended to the desired state, it is clamped and a seed crack is initiated by cutting the sheet with a blade (white line, towards left of frame). A square grid is drawn on the sheet before it is stretched in order to measure the extension level as rubber is stretched.

Here $\vec{u}(\vec{r})$ describes the distance from the origin of a mass point that was located at $\vec{r}$ when the rubber was relaxed.

An effective two-dimensional Mooney-Rivlin theory was adopted to describe the elastic behavior of thin rubber sheets [40]:

$$U/\rho = e_{\mathrm{MR}} = a\left[I_1 + 2bI_2 + E_{zz}(1 + 2bI_1)\right], \tag{2.2}$$

where U has units of energy per volume, a is a constant with units of velocity squared, b is a dimensionless constant, $I_1 = E_{xx} + E_{yy}$, and $I_2 = E_{xx}E_{yy} - E_{xy}^2$, and

$$E_{zz} = \tfrac{1}{2}\left(\frac{1}{4I_2 + 2I_1 + 1} - 1\right). \tag{2.3}$$

The numerical approach is to consider microscopic interactions between

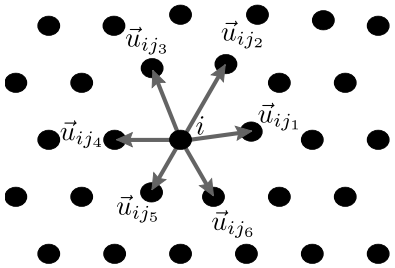

Figure 2.2: Diagram showing triangular lattice of lattice spacing Δ.

mass points in a discrete lattice model that produce the rubber constitutive equation, eq. (2.2) in the continuum limit, but break when the separation between mass points is large enough. The lattice model is made up of a two-dimensional network of mass points which are connected with elastic bonds to six nearest neighbors to form a triangular lattice as shown in fig. 2.2. Take the original bond length between particles i and j to be Δ_{ij}. To obtain a numerical expression of the strain invariants, let $\vec{u}_{ij} \equiv \vec{u}_j - \vec{u}_i$, let $n(i)$ refer to the nearest neighbors of i, and define

$$F_i = \frac{1}{6} \sum_{j \in n(i)} \begin{cases} \left(\vec{u}_{ij} \cdot \vec{u}_{ij} / \Delta_{ij}^2 - 1 \right) & \text{if} \quad u_{ij}/\Delta_{ij} < \lambda_f, \\ \lambda_f^2 - 1 & \text{else,} \end{cases} \tag{2.4}$$

$$K_i = \begin{cases} \frac{1}{18} \sum\limits_{j,k \in n(i); j \neq k} \frac{(\vec{u}_{ij} \times \vec{u}_{ik})^2}{\Delta_{ij}^2 \Delta_{ik}^2} & \text{for } K_i < K_{\max}, \\ K_{\max} & \text{else.} \end{cases} \tag{2.5}$$

The quantity K_i has not previously been introduced in publications on

this method [40]. From these numerical quantities, one can form representations of the strain invariants as follows:

$$I_1^i = F_i, \tag{2.6}$$

$$I_2^i = K_i/4 - F_i/2 - 1/4, \tag{2.7}$$

and finally construct the energy from

$$U = \sum_i m\, e_{\mathrm{MR}}\left(I_1^i, I_2^i\right), \tag{2.8}$$

where m is the mass in a unit cell, and the energy density e_{MR} is given by eq. (2.2).

In the continuum limit,

$$\begin{aligned} K_i &= \frac{1}{18} \sum_{j,k\in n(i);j\neq k} \frac{(\vec{u}_{ij} \times \vec{u}_{ik})^2}{\Delta_{ij}^2 \Delta_{ik}^2} \\ &= (2E_{xx}+1)(2E_{yy}+1) - (2E_{xy})^2 = 4I_2 + 2I_1 + 1. \end{aligned}$$

From eq. (2.3), $K_i = 1/(2E_{zz}+1) \approx \lambda_z^{-2}$; K_i is approximately the inverse square of the extension ratio in thickness direction λ_z.

If the criterion for rupture is that λ_f is a constant, then cracks in numerical rubber undergo a tip-splitting instability well below the shear wave speed that prevents them from reaching supersonic speeds. To account for experimental observations in rubber, it is necessary to suppress these instabil-

ities. This task was accomplished previously in an *ad hoc* way by making the bonds into a node tougher when two of the bonds attached to it had already broken [40]. Making use of the physical interpretation of K_i a failure criterion that makes physical sense and leads to the desired type of toughening is posited. The failure criterion is

$$\lambda_f = \lambda_f^0 + g/K \approx \lambda_f^0 + g\lambda_z^2. \tag{2.9}$$

Here λ_f^0 and g are constants. The failure criterion can be interpreted as saying that the sheet ruptures more easily when it has been stretched thin. The particular functional form $1/K_i$ is chosen for simplicity absent any direct evidence that another form should be preferred. The way this failure criterion stabilizes crack tips is that in the wake of the tip, the rubber contracts perpendicular to the direction of crack motion, and by contracting becomes thicker and therefore tougher. Numerical simulation bears out this physical reasoning, since simulations using eq. (2.9) in fact can produce supersonic cracks.

The complete equation of motion of particle i reads

$$m\frac{\partial^2 u_i^\alpha}{\partial t^2} = -\frac{\partial U}{\partial u_i^\alpha} - \beta\frac{\partial^2 U}{\partial t \partial u_i^\alpha}, \tag{2.10}$$

where the final term represents Kelvin dissipation with a dissipation parameter, β. The fact that nothing but dissipation is added to the equation of motion

is a severe simplification. Rubber is hysteretic, and its strain-rate dependence is much more complicated than can be captured by a Kelvin model [43, 45, 46]. However it appears that the very simple choice of dissipation allows adequate comparison with the collection of experiments described here.

2.4 Determination of parameters

The experimentally determined sound speeds (or elastic modulus) are used to calibrate the Mooney-Rivlin model [53]. Experimentally, the dimensionless parameter b in eq. (2.2) is 0.053 (at 24 °C) , so in a first theoretical account one can set $b = 0$. In this approximation the Mooney-Rivlin energy density e_{MR} reduces to the Neo-Hookean energy density

$$e_{\mathrm{MR}} \approx e_{\mathrm{NH}} = a\big(I_1 + E_{zz}\big). \tag{2.11}$$

This simple expression provides an adequate although not exceeding accurate description of rubber over the range of extensions in the experiments. The parameter a is directly related to sound speeds. It is obtained through fits to stress *vs.* extension in the range where the extension ratio λ_y range from 1 to 2. Reference [53] showed in experiments at 24 °C that this procedure is in good accord with time-of-flight measurements. Stress-extension curves were also measured at 85 °C and the result suggests that sound speed increases slightly above the room temperature value [7]. In simulations $a = 686.44$ $(\mathrm{m/s})^2$ and c_s=26.2 m/s are used at the temperature of 85 °C.

The simulations still depend upon three unknown parameters β, λ_f^0, and g. The dissipation parameter β was obtained from experiments in which bands of rubber were allowed to undergo free retraction. This was done by stretching a rubber band, releasing it, waiting for a retraction front to develop, and measuring its acceleration with video images [47]. These results were compared with direct numerical simulations using eq. (2.10). The parameter β was modified in simulations until the calculated peak acceleration of the simulations matched the peak acceleration of the experiment. Since no bonds break in a retraction simulation, the only tunable parameter is β.

The only parameter in simulations not directly obtained from experiments is the failure extension ratio λ_f consisting of two components: the cutoff constant λ_f^0 and the coefficient g in the toughening rule of eq. (2.9). By fitting experimental and numerical crack speeds, $\lambda_f^0 = 4.1$, and $g = 100$ were obtained. Results are quite insensitive to the value of g so long as it is large enough to keep the crack tip stable.

Assembling all experimentally derived parameters, simulations were performed with values of $a = 686.44$ (m/s)^2, b=0, $\beta = 9 \times 10^{-6}$ s, and rupture extension $\lambda_f = 4.1 + 100\lambda_z^2$. Three numerical systems with heights of 180, 360, and 630 rows were tested to match the actual specimens with 5.1 cm, 10.2 cm, and 17.8 cm height respectively. The system was at least five times as wide as it is tall in the unstretched state. The system ran for more than 15000 time units (>0.2 s) to ensure it has approached a steady state.

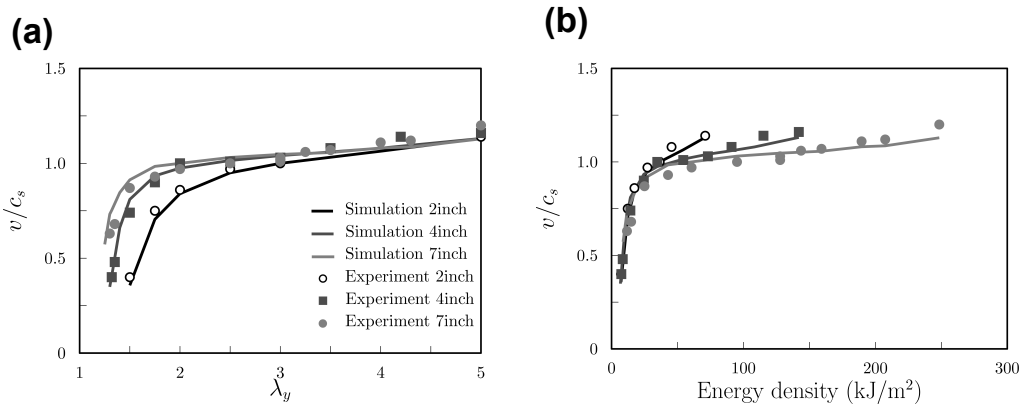

Figure 2.3: Crack speed scaled by the shear wave speed as a function of the extension ratio λ_y in (a); and of the elastic energy density in (b). Both experimental results and simulations show two different scaling regimes for the crack speed. When Mooney-Rivlin constant b is varied between 0 and 0.053, the numerical crack speeds only vary by 10%. All crack speeds are determined within the experimental error of ± 0.75 m/s.

2.5 Results and discussion

In this section, the crack speeds from the simulations are compared with those form the experiments. For a Mooney-Rivlin material, longitudinal wave speed depends strongly on extension but shear wave speed (c_s) behaves like a constant when extensions λ_x and λ_y on the order of 2 or greater [40]. Therefore it makes sense to measure crack speeds in rubber in units of the shear wave speed. The experimental and numerical crack speeds, scaled by the shear wave speed (c_s=26.2 m/s at 85 °C), are plotted as a function of extension ratio λ_y in fig. 2.3(a) and of the elastic energy density in fig. 2.3(b). Here, the elastic density is calculated as $E = \rho e_{\mathrm{NH}}(\lambda_y)\, h/\lambda_y$, where h is the height of the sample and e_{NH} is the Neo-Hookean elastic energy density as

shown in eq. (2.11). Figure 2.3 shows that the numerical results based on the Neo-Hookean model are in agreement with the laboratory measurements. As expected, both subsonic cracks ($v < c_s$) and supersonic cracks ($v > c_s$) are observed in three different sized samples. The transition from subsonic cracks to supersonic cracks occurs at about $\lambda_y = 2.0$ for the largest sample with 17.8 cm height, $\lambda_y = 2.5$ for sample with 10.2 cm height, and $\lambda_y = 3.0$ for sample with 5.1 cm height.

As predicted by supersonic rupture theory, there are two different scaling regimes for the crack speeds [40]. For subsonic cracks, crack speeds are independent of system size when plotted as a function of the elastic energy density E. This is the prediction of linear elastic fracture mechanics, worked out for example for cracks in strips by Marder [37] and verified in detail by Goldman et al. [24]. However, supersonic cracks in rubber sheets have quite different characteristics. Their crack speeds become independent of system size when plotted *vs.* λ_y rather than *vs.* elastic energy density shown in fig. 2.3. There is so much elastic energy stored in the vicinity of crack tip that it can support supersonic crack propagation and even provide extra energy to flow outwards. The crack speed is no longer limited by the time taken for the elastic energy from far away to flow into the crack tip [4].

Furthermore, crack openings have a qualitatively different shape in two scaling regimes. Subsonic cracks have a parabolic tip as expected and the opening increases as λ_y increases; on the other hand, supersonic cracks have a wedge-like opening, with an opening angle of about 150° in experiment and

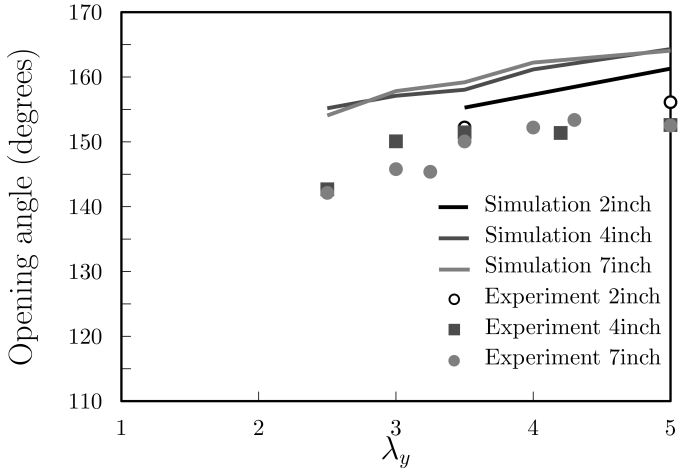

Figure 2.4: Comparison of the rupture opening angles for supersonic cracks obtained from experimental results and numerical runs based on the Neo-Hookean energy model over a range of states where the extension ratio λ_y lies between 2.5 and 5. The simulations overestimate the angles around 10° systematically in all three sized samples.

160° from numerics as shown in fig. 2.4. Figure 2.5 shows experimental and numerical measurements of velocity fields around a crack tip. The simulations slightly overestimate the openings and particle velocity, but otherwise theory and experiment correspond well.

2.6 Conclusion

The properties of cracks in rubber at a temperature of 85 °C were measured and the transition between subsonic and supersonic cracks was studied. Numerical simulations based on a Neo-Hookean theory with Kelvin dissipation and a new rule for increasing toughness were conducted. This simple model

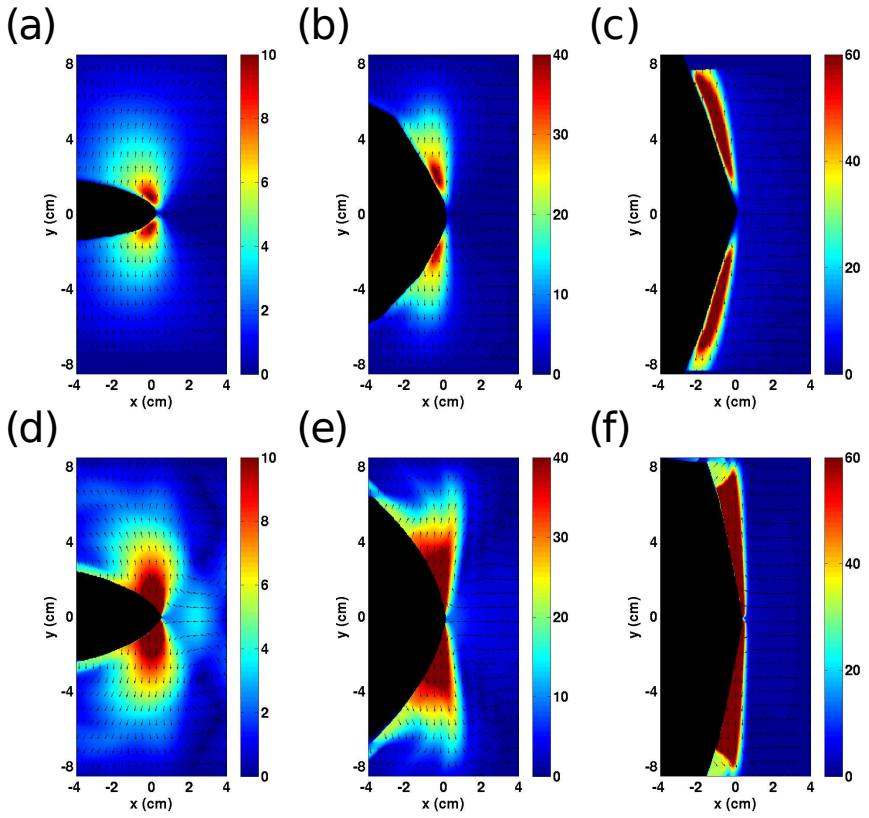

Figure 2.5: Top panels: images showing the experimental particle velocity fields of three steadily propagating cracks in h=17.8 cm specimens: (a) $\lambda_y = 1.3$ and $v = 0.63\, c_s$; (b) $\lambda_y = 1.75$ and $v = 0.93\, c_s$; (c) $\lambda_y = 3.0$ and $v = 1.02\, c_s$. The bottom panels show the particle velocity image of simulations compared to three experimental results which have the same crack speeds within 3% and extension ratios (d) $\lambda_y = 1.27$ and $v = 0.63\, c_s$; (e) $\lambda_y = 1.6$ and $v = 0.95\, c_s$; (f) $\lambda_y = 3.0$ and $v = 1.047\, c_s$. Cracks propagate to the right, and black regions are the actual opening. The color scale is coded according to the particle velocity and arrows show the direction of particle motion. We note that the particle velocity close to the crack tip is falsely represented in (c), because the velocity gradient in these regions is so large that Particle Image Velocimetry (PIV) algorithm cannot yield reliable results. The particle velocity fields in simulations are similar to those in experiments, but the opening angles of the ruptures are slightly larger than experimental results. Wedge-like openings are observed as $\lambda_y = 3.0$ in both experimental results (c) and simulations (f).

produces satisfactory agreement with experiment for crack speeds and particle velocity fields. The experiments provide the first confirmation that supersonic cracks obey a scaling law in which speed naturally depends upon strain rather than energy density. The validity of this new scaling law implies that there exists a small characteristic scale length related to dissipative processes $\sim (\beta v)$ which is not present in linear elastic fracture mechanics, a scale-free theory. Remaining quantitative inaccuracies, such as overestimation of opening angles and particle velocity, are likely related to the very simple equation of motion, eq.(2.10), employed for the simulations.

Chapter 3

Theory of Oscillating Cracks

3.1 Introduction

The theory of fracture mechanics is worked out in greatest detail for single cracks moving in a straight line. However cracks can create much more complicated geometrical patterns, including complex branched structures. The simplest deviation from straight motion occurs when a crack starts to oscillate. Oscillations are not seen very widely, but Deegan et al. [13] found them in rubber, and Livne et al. [35] found them in gels (fig. 3.1). In gels, the experimental results show that the critical crack speed at the onset of oscillations is about 90% of the shear wave speed; in rubber, the main experimental findings are a phase diagram for oscillations as a function of biaxial loading, and measurements of amplitude and wavelength of oscillation once the wiggling begins (fig. 3.2). Bouchbinder et al. [3] provided a theory for the onset of oscillations in gels, but the oscillation of cracks in rubber has not been explained. The goal of this study is to provide an explanation.

A source of difficulty that has prevented the analysis of cracks in rubber is lack of certainty about the equation of motion governing the crack tip. For

a crack moving in a straight line in a crystal it is possible for simple model potentials to describe crack motion in full atomic detail, and with more realistic potentials that same task can be carried out numerically. However for any material more complex than a single crystal, and in all cases as soon as a crack deviates from a straight line, rules for crack tip motion can no longer be obtained from microscopic physics.

One can turn to other types of argument to derive rules for crack tip motion. Energy conservation provides a powerful constraint on how cracks move, and arguments about the symmetry of crack tip fields have led to the principle of local symmetry [25], which has gathered considerable experimental support for cracks not moving too fast. The whole situation is much more uncertain for cracks moving quickly; say, above 20% of the shear wave speed. There are numerous proposals for equations of motion, but the technical difficulty of employing them in calculation combined with the uncertainty about which if any is correct has meant that the original problem of explaining when cracks in rubber begin to oscillate has remained unsolved.

This study develops a theory that bypasses these difficulties. This theory recovers the onset of oscillations in gels in a somewhat simpler way than has been found before. We present a way to describe the phase diagram of oscillating cracks in rubber that requires almost no knowledge of the equation of motion altogether. Nevertheless, the seemingly insignificant constraints one must impose suffice to rule out most of the equations of motion that had previously been guessed, while a simple equation of motion that is compatible

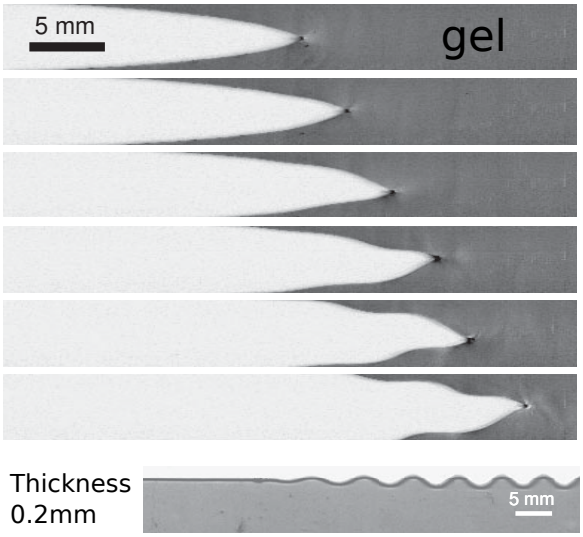

Figure 3.1: A sequence of photographs of a oscillating crack in gels. Adapted from [35].

with the constraints had not been guessed before.

3.2 Background

This section presents a comparison of oscillating cracks in gels and those in rubber and the background information of this study.

3.2.1 Gels and rubber experiments

The results from Deegan et al. [13] and Livne et al. [35] suggest some similarities between the oscillating cracks in gels and those in rubber. First, oscillating cracks in both gels and rubber are fast cracks; the critical crack speed at the onset of oscillations is 90% of the shear wave speed c_s or more.

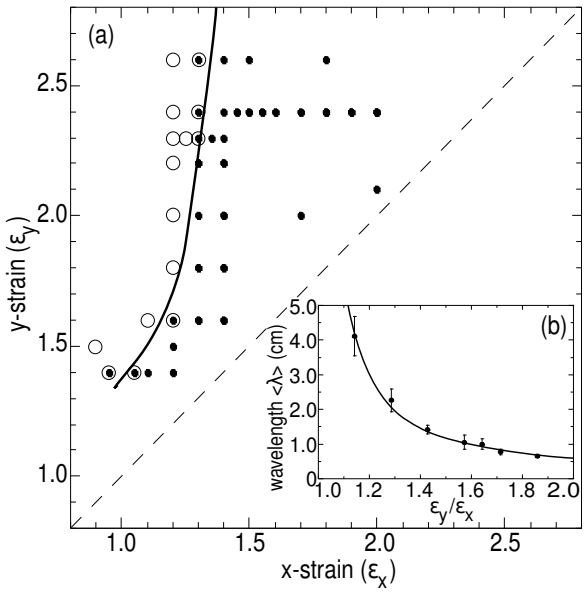

Figure 3.2: (a) A phase diagram of two possible crack shapes observed in experiments: oscillations • and straightness in ∘, as a function of biaxial loading. Ambiguous points ⊙ represent both straightness and oscillations observed in different runs with the same initial conditions. (b) A plot of wavelength as a function of $\varepsilon_y/\varepsilon_x$ [13]. The experiments were conducted with thin rubber sheets under the strain state $(\varepsilon_x, \varepsilon_y)$, where ε_x is the strain along the x-direction and ε_y is the strain along the y-direction.

Second, their results show that these oscillating cracks found in very thin films where the typical sample thickness is about 0.2 mm and the typical sample height and sample length are on the order of 100 mm. In other words, the sample thickness is merely a few thousandths of the sample height. Besides, the out-of-plane motion is insignificant in this study based on the fact that oscillating cracks observed in experiments that were designed to reduce the out-of-plane motion by clamping the rubber sheet between two glass plates [13]. Thus, it is reasonable to assume that these oscillating cracks are two dimensional.

On the other hand, their studies reveal some significant differences. Oscillating cracks in gels were observed under uniaxial loading at strain between $10-20\%$ but oscillating cracks in rubber were found only under biaxial loading at strains on the order of 100%. Besides, the wavelength of oscillating cracks in gels is a few percent of the sample height but the wavelength of oscillating cracks in rubber ranges from 10-50% of the sample height.

3.2.2 Three conventional fracture modes

Based on the symmetrical ways of loading around crack tip relative to the crack faces, cracks can be classified into three independent modes, as shown in fig. 3.3. In Mode I (opening mode), the loading is perpendicular to the crack faces. In mode II (sliding mode), the loading is parallel to crack faces and perpendicular to the crack front. In mode III (tearing mode), the loading is parallel to both the crack faces and the crack front. Thus, a real

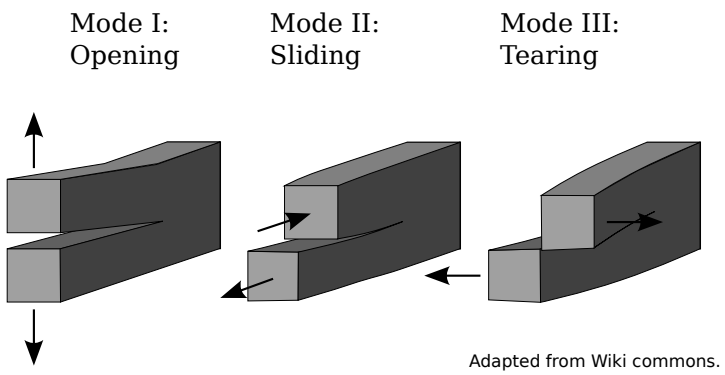

Figure 3.3: The three conventional modes of fracture: Model I-opening, Mode II-shearing and Mode III-tearing. Adapted from Wiki commons.

fracture can be described by some combinations of these three modes.

According to the discussion above, the out-of-plane motion is irrelevant here. This study is focused on mixed modes I and II cracks growth in the xy plane.

3.2.3 Stress intensity factors

Linear elastic fracture mechanics assumes that all complex nonlinear and dissipative processes occurred in a region of negligible size around a crack tip (the fracture process zone), and materials are linearly elastic outside of this region [8, 18]. In 1957, Irwin first proposed a universal singularity of stress fields in the region surrounding the tip but outside of the fracture process zone [31]. For a two dimensional crack propagating in the xy plane, the near-tip stress fields in polar coordinates (r, ϕ), with the origin at the crack tip can be

expressed as [8, 18]

$$\sigma_{ij}(r,\phi) \sim \frac{K_I}{\sqrt{2\pi r}} f_{ij}^{I}(v,\phi) + \frac{K_{II}}{\sqrt{2\pi r}} f_{ij}^{II}(v,\phi).$$

Here $r \equiv \sqrt{(x-x_{\text{tip}})^2 + (y-y_{\text{tip}})^2}$, $\phi \equiv \text{atan}\left[(y-y_{\text{tip}})/(x-x_{\text{tip}})\right]$, i and j range over x and y, and v is the crack speed. $K_{I,II}$ represent the stress intensity factor for mode I and mode II, respectively and these stress intensity factors contain all details of loading geometries size and loading history [8, 18]. $f_{ij}^{I,II}(v,\phi)$ are some known dimensionless universal functions [8, 18].

3.3 Oscillating cracks in gels

One of the central findings of fracture mechanics is that stress fields around a two-dimensional crack tip moving at some velocity v adopt a universal form, in which the stresses around a crack are the sum of two spatial fields of different symmetry, multiplied by two constants, the stress intensity factors K_I and K_{II}, that provide the amplitudes of the two fields. Since the crack tip is enveloped by this spatial stress field, knowledge of the field, and thus the two constants, should suffice to describe the speed and direction of the crack tip. The stress fields arise in response to external loads on the fracture system and the motion of the crack. Thus there are two basic equations that describe crack motion. A first equation describes how the crack tip responds to stresses around it. The second equation describes how stresses around the crack tip arise in response to the crack motion. It is natural when trying to describe

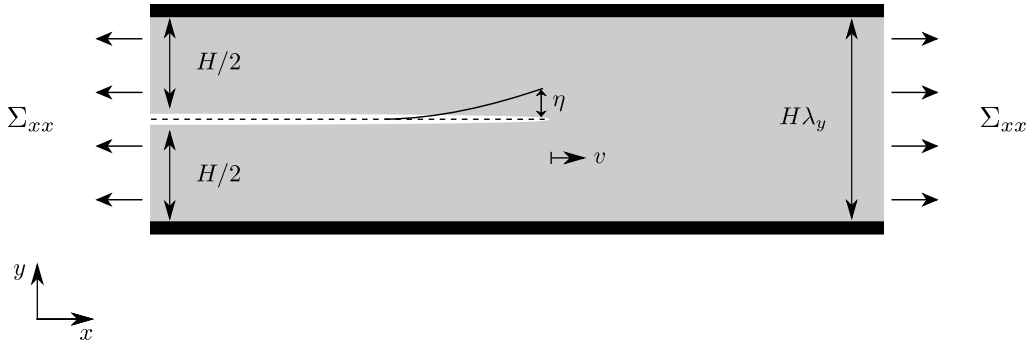

Figure 3.4: Schematic illustration of system setup. The dashed line is the path of a perfectly straight crack along the x-axis and the solid line is the path of a curved crack. Let η describe the deviation between the curved crack and the straight crack. The original height of the strip is H and the sample height under deformed is $H' = \lambda_y H$. During rupturing, the upper and lower edges of the strip are held fixed by a rigid grip, and the remote stress along x-axis is Σ_{xx} at all times.

crack dynamics to begin with the first equation, describing response of tip to stress fields. However, since the correct equation is particularly uncertain for cracks in polymeric systems, we start with the second in this study.

3.3.1 System setup

Consider a slightly curved or kinked crack. These have been studied with a perturbation analysis about the reference solutions for a perfectly straight crack [11, 19, 32]. In particular, consider a semi-infinite perfectly straight crack running to the right along the x-axis at speed v in an infinite strip, as shown in fig. 3.4. The strip is stretched to a desired extension state (λ_x, λ_y), where λ_x and λ_y are the extension ratios along the x direction and the y direction, respectively. The original height of the strip is H. The

height of the deformed sample is H' and we have $H' = \lambda_y H$. Let Σ_{xx} and Σ_{yy} represent the stresses far to the right along the x direction and the y direction, respectively. During rupturing, the upper and lower edges of the strip are held fixed by a rigid grip, and the remote stress along x-axis remains Σ_{xx} at all times. The symmetry of the loading is such that the only nonzero stress intensity factor is $K_I = K_I^0$.

3.3.2 Stress intensity factors

Consider a curved crack slightly deviating from the perfectly straight crack. Let $\eta(x)$ describe the deviation of the curved crack from the x-axis, and let $\theta(x)$ describe the tangent angle of crack measured from the x-axis. Suppose the amplitude of η is much smaller than the sample size or crack length. In the following analysis, η is used as the perturbation parameter and $\theta(x) \approx \partial\eta/\partial x$. For linear elastic materials, Cotterell and Rice [11] found expressions for the coefficients of the stress field accurate to first order in η. They are

$$K_I(x) = K_I^0, \tag{3.1}$$

and

$$K_{II}(x) = \frac{\theta(x)}{2} K_I^0 - T\sqrt{\frac{\pi}{2}} \int_{-\infty}^{x} \frac{\theta(\xi)}{\sqrt{x-\xi}} d\xi. \tag{3.2}$$

Here x is the location of the crack tip, and T, called T-stress, is a non-singular local stress parallel to the crack. For a linear elastic material with stresses Σ_{xx} and Σ_{yy} imposed far from the crack, we have $T = \Sigma_{xx} - \Sigma_{yy}$ [11, 14].

Now, consider a linear mode $\eta_q(x) = \eta_0 e^{qx}$, where $\eta_0 \ll H$. Thus, $\theta_q(x) = \partial\eta_q/\partial x = \theta_q(0)\, e^{qx}$. Let $x' = x - \xi$ and rewrite eq. (3.2) as:

$$\begin{aligned} K_{II}(x) &= \frac{\theta_q(x)}{2} K_I^0 - T\sqrt{\frac{\pi}{2}} \int_{-\infty}^{x} \frac{\theta_q(\xi)}{\sqrt{x-\xi}} d\xi \\ &= \frac{\theta_q(x)}{2} K_I^0 - T\sqrt{\frac{\pi}{2}} \int_{-\infty}^{x} \frac{\theta_q(0)\, e^{q\xi}}{\sqrt{x-\xi}} d\xi \\ &= \frac{\theta_q(x)}{2} K_I^0 - T\sqrt{\frac{\pi}{2}} \theta_q(x) \int_{0}^{\infty} \frac{e^{-qx'}}{\sqrt{x'}} dx' \\ &= K_I^0 \left(\frac{1}{2} - \frac{T}{K_I^0}\sqrt{\frac{2}{q}} \right) \theta_q(x). \end{aligned} \tag{3.3}$$

3.3.3 Energy release rate criterion and generalized force

A maximum energy release rate criterion is proposed here to determine crack tip motion. Consider a mixed-mode 2-dimensional crack growing at the speed of v in the xy plane. Let $\vec{e}_1$ and $\vec{e}_2$ represent unit vectors tangential and normal to the crack growth direction, respectively. An energy flow vector $\vec{\omega} = \omega_1 \vec{e}_1 + \omega_2 \vec{e}_2$ can be found by using Eshelby's energy-momentum tensor [2, 49]. Here ω_1 represents the conventional dynamic energy release rate, and ω_2 represents the energy changes caused by a small virtual displacements of the crack tip along a direction normal to the crack surfaces. For a crack in a linear elastic medium, one has [2, 38, 49]

$$\omega_1(v) = \frac{A(v)}{2\mu} \left(\alpha_d K_I^2 + \alpha_s K_{II}^2 \right), \tag{3.4}$$

$$\omega_2(v) = -\frac{B(v)}{2\mu} K_I K_{II}. \tag{3.5}$$

Here μ is the shear modulus, c_s and c_d are the shear wave speed and the dilatational wave speed, respectively, $\alpha_s = \sqrt{1 - v^2/c_s^2}$, $\alpha_d = \sqrt{1 - v^2/c_d^2}$, $R = 4\alpha_d\alpha_s - (1 + \alpha_s^2)^2$, $A(v) = (1 - \alpha_s^2)/R$ and $B(v) = 2\alpha_s\alpha_d(\alpha_d - \alpha_s)(1 - \alpha_s^4)/R^2$.

A general energy release rate G is the energy required to create a unit of new surface area for a crack propagating along a direction of $\hat{t} = (\cos\phi, \sin\phi)$, where ϕ is an arbitrary angle measured from the current crack direction. Thus, from eq. (3.4) and eq. (3.5), one can obtain $G = \vec{\omega} \cdot \hat{t} = \omega_1 \cos\phi + \omega_2 \sin\phi$ [38]. Based on a maximum energy release rate criterion, a crack prefers to choose the direction where energy release rate is maximum, i.e., $\partial G/\partial\phi = 0$. Thus, a generalized force driving the rotational motion of crack can be defined as

$$F \equiv \left.\frac{\partial G}{\partial \phi}\right|_{\phi=0} = -\frac{B(v)}{2\mu} K_I K_{II}, \tag{3.6}$$

where K_I and K_{II} are held constant when the partial derivative is taken. For convenience, let's define a dimensionless force $f = F/F_0$, where F_0 has units of F. Without loss of generality, choose $F_0 = K_I^2/2\mu$ to obtain

$$f = -B(v)\, K_{II}/K_I. \tag{3.7}$$

3.3.4 Modified principle of local symmetry

Suppose the time rate of change in crack direction is proportional to f, that is $\partial\theta/\partial t \propto f$. Then the rotational motion of the crack is described by

$$\tau\frac{\partial\theta}{\partial t} = f = -B\left(v\right)\frac{K_{II}}{K_I}, \tag{3.8}$$

with a proportional coefficient τ which has units of time. The maximum energy release rate criterion provides a physical explanation for crack tip motion and the law, eq. (3.8), agrees with the principle of symmetry [25, 27].

Let ds describe the crack advance distance, i.e., $ds = vdt$. The crack is assumed to be slightly curved, so $ds = \sqrt{\left(dx\right)^2 + \left(dy\right)^2} \approx dx$. Employ $v\partial/\partial x \simeq \partial/\partial t$, and then eq. (3.8) becomes

$$\mathcal{D}\frac{\partial\theta}{\partial x} = f = -B\left(v\right)\frac{K_{II}}{K_I}, \tag{3.9}$$

where $\mathcal{D} = v\tau$.

The underlying assumption in Linear elastic fracture mechanics is that all complex nonlinear and dissipative processes occurred in a region of negligible size around a crack tip (the fracture process zone), and materials are linearly elastic outside of this region. However, recent studies suggest that this assumption becomes questionable for cracks traveling above 20% of the shear wave speed [3–6, 36].

In order to consider the mechanisms in the fracture process zone, a

more general model for crack motion is proposed in the following equation:

$$\mathcal{D}\frac{\partial\theta}{\partial x} \sim \overline{f}, \tag{3.10}$$

where $\overline{f}$ is a convolution of f and a weighting function, Φ. That is,

$$\overline{f}\,(x) \equiv \int_{-\infty}^{\infty} d\xi \Phi\,(\xi)\, f\,(x-\xi)\,. \tag{3.11}$$

This idea allows that the weighting function contains all the details of the fracture process zone. There are two constraints for Φ. First, $\Phi(x)$ must vanish for $x < 0$ based on causality. Second, the weighting function Φ is normalized, i.e., $\int_{-\infty}^{\infty} dx\Phi\,(x) = 1$. When choosing $\Phi\,(x) = \delta\,(x)$, eq. (3.10) becomes the conventional principle of local symmetry.

From eq. (3.1), eq. (3.3) and eq. (3.7), the equation of motion in eq. (3.10) becomes

$$\mathcal{D}\frac{\partial\theta_q\,(x)}{\partial x} = -B\,(v)\,\frac{K_{II}\,(x)}{K_I^0}\tilde{\Phi}\,(q)\,, \tag{3.12}$$

where

$$\tilde{\Phi}\,(q) \equiv \int_0^{\infty} dx'\Phi\,(x')\,e^{-qx'}. \tag{3.13}$$

3.3.5 Time delay model

The mechanisms in the fracture process zone around the crack-tip can play important roles for fast cracks in gels [6, 36]. Bouchbinder suggests that the oscillatory instability in gels is originated from a delay time associated with

the causality between the stress fields outside of the fracture process zone and crack tip motion [3]. To describe the delay time due to causality, the most simple but plausible weighting function $\Phi(x) = \delta(x - \ell_{\mathrm{p}})$ is used in this model.

In the experiments of [35], the wavelength of oscillations $\Lambda \sim 7.5$ mm and the sample height H =115 mm, that is $\Lambda/H \sim 7\%$. It is reasonable to assume that $\Lambda \ll H$ and then the second term on the right hand side in eq. (3.3) can be ignored (see Section A). Equation (3.12) becomes

$$q = -\frac{B\,(v)}{2\mathcal{D}} e^{-q\ell_{\mathrm{p}}}. \tag{3.14}$$

The main question is when eq. (3.14) first has a solution where the real part of q is positive. This happens when the real part vanishes, so $q\ell_{\mathrm{p}} = -i\pi/2$. Given $\mathcal{D} = 0.8\ell_{\mathrm{p}}$ and $c_d/c_s = 2$ (same ratio of c_d to c_s for the materials used in [35]), eq. (3.14) predicts that the critical crack speed at the onset of oscillations is $v = 0.8c_s$. This time delay model agrees well with experiments ($v = 0.9c_s$ at onset) [35] and analytic predictions ($v = 0.77c_s$ at onset) [3]. The wavelength at the onset of oscillations predicted by this model is $\Lambda = 4\ell_{\mathrm{p}}$ so that we estimate the size of the fracture process zone $\ell_p \sim 1$ mm, which agrees with previous studies [3, 6, 36].

3.4 Oscillating cracks in rubber

Based on the discussion above, we know that oscillating cracks in rubber are different from those in gels: in rubber, oscillating cracks were only found under biaxial loading, and the wavelength of these oscillations is comparable with the sample height.

This section presents a nonlinear elasticity model for rubber, a phase diagram for oscillations as a function of biaxial loading, and an overdamped oscillation model for oscillations in rubber.

3.4.1 Neo-Hookean model

We assume that rubber is Neo-Hookean, so that the energy of a uniform sample in biaxial strain is (up to an additive constant U_0) [39, 40, 42]

$$U = \frac{\mu}{2}\left[\lambda_x^2 + \lambda_y^2 + 1/\left(\lambda_x^2\lambda_y^2\right)\right] + U_0. \tag{3.15}$$

Here $\vec{u}\,(\vec{r})$ is the distance between the origin and a mass point that was originally at $\vec{r}$, and μ is the shear modulus.

The experiments we discuss take place for extensions on the order of 2 or more [13], allowing us to neglect the final term in eq. (3.15) except in the wake of the crack where the rubber has relaxed to a state described by $\lambda_x^r = \lambda_x$ and $\lambda_y^r = 1/\sqrt{\lambda_x}$, which minimizes the energy in λ_y when λ_x is held constant. The stress intensity factor for a straight crack is $K_I^0 = \mu\sqrt{\alpha_s H\left(\lambda_y^2 - 2/\lambda_x\right)}$ (see Section B). Outside of the fracture process zone, the experimental results show

that the change in $u_x(x,y)$ is insignificant during rupturing, so one can assume that $u_x(x,y) = \lambda_x x$ at all times [39, 40]. Thus, the T-stress is $T = \Sigma_{xx} = \mu\lambda_x$.

Based on the similar analysis described above, for a slightly curved crack, the expressions for the coefficients of the stress field accurate to first order in η are (see Section C)

$$K_I(x) = K_I^0, \tag{3.16}$$

and

$$K_{II}(x) = \theta(x) K_I^0 - T\sqrt{\frac{\pi}{2}} \int_{-\infty}^{x} \frac{\theta(\xi)}{\sqrt{x-\xi}} d\xi. \tag{3.17}$$

It is worth noting that there are two differences between eq. (3.2) and eq. (3.17). First, the first term on the right hand side is one half in eq. (3.2) but unity in eq. (3.17). Second, $T = \Sigma_{xx} - \Sigma_{yy}$ in eq. (3.2) but $T = \Sigma_{xx}$ in eq. (3.17).

From eq. (3.10), eq. (3.16) and eq. (3.17), the equation of motion for a linear mode $\eta_q = \eta_0 e^{qx}$ is

$$\mathcal{D}\frac{\partial\theta_q(x)}{\partial x} = -B(v)\left(1 - \frac{T}{K_I^0}\sqrt{\frac{2}{q}}\right)\theta_q(x)\tilde{\Phi}(q),$$

or

$$\mathcal{D}q = -B(v)\left(1 - \frac{T}{K_I^0}\sqrt{\frac{2}{q}}\right)\tilde{\Phi}(q). \tag{3.18}$$

Unlike the analysis for oscillating cracks in gels, the term led by T/K_I^0

in eq. (3.18) cannot be ignored because the sample height and wavelength of oscillations are comparable. Given $H' = 10$ cm and the critical crack speed at the onset of oscillations in rubber $v = 0.96c_s$, we note that the phase boundary in the phase diagram for oscillating cracks in rubber [13] obeys the constraint $T/K_I^0 \approx 2.72/\sqrt{H'}$, as shown in fig. 3.5. Because T and K_I^0 are parameters that depends only on the loading states and the material properties of rubber, this constraint suggests that it requires almost nothing about the equation of motion to describe the shape of the phase diagram.

In order to explain the oscillations in rubber experiments, let's rewrite (3.18) as:

$$\Psi(q) = \frac{T}{K_I^0}, \tag{3.19}$$

where

$$\Psi(q) = \sqrt{\frac{q}{2}}\left(1 + \frac{q\mathcal{D}}{\tilde{\Phi}(q)\, B(v)}\right). \tag{3.20}$$

The right hand side of eq. (3.19) is just a constant at the onset of oscillations. That is, $\Psi(q)$ reaches a particular real positive value for oscillations to begin and the constraints in $\Psi(q)$ are sufficient to rule out the time delay model, $\Phi(x) = \delta(x - \ell_{\mathrm{p}})$, which is proposed for the oscillations in gels.

3.4.2 Overdamped oscillation model

An overdamped oscillation model that satisfies the constraints in $\Psi(q)$ and covers the phase diagram is proposed for oscillating cracks in rubber. In

this model, the equation of motion reads

$$\frac{\partial^2 K_{II}}{\partial t^2} = -b\frac{\partial \theta}{\partial t} - \Omega_0^2 K_{II}. \tag{3.21}$$

Based on an analogy to a mass-spring-damper system, this model considers a force law associated with a second time derivative of K_{II} (acceleration) that is proportional to $-K_{II}$ (a restoring "force" due to a curved crack), and a dissipative force that has the form of $-b\partial\theta/\partial t$, where b and Ω_0 are two material dependent, positive constants.

Define two dimensionless parameters, $b' = b\tau/K_I^0$ and $\Omega_0' = \Omega_0\tau$. Nondimensionalize eq. (3.21) for the linear mode $\eta_q(x)$ to have

$$\mathcal{D}\frac{\partial \theta_q}{\partial x} = -\left[\frac{\left(\Omega_0'\right)^2 + q^2\mathcal{D}^2}{b'}\right]\left(1 - \frac{T}{K_I^0}\sqrt{\frac{2}{q}}\right)\theta_q(x). \tag{3.22}$$

From eq. (3.22), we have

$$\Psi(q) = \sqrt{\frac{q}{2}}\left[1 + \frac{b'q\mathcal{D}}{\left(\Omega_0'\right)^2 + q^2\mathcal{D}^2}\right]. \tag{3.23}$$

The wavelength of oscillations can be estimated based on the following considerations. At the onset of oscillations, q is a imaginary number, i.e., $q = ik_c$, where $k_c > 0$, and $\Psi(q) = 2.72/\sqrt{10\text{ cm}}$. From eq. (3.19) and eq. (3.23), one can conclude that $b' = \left[k_c^2\mathcal{D}^2 - \left(\Omega_0'\right)^2\right]/(k_c\mathcal{D})$ and $k_c = \Psi(q)^2 = \left(2.72/\sqrt{10\text{ cm}}\right)^2$. Thus, the wavelength of oscillations at the onset of oscilla-

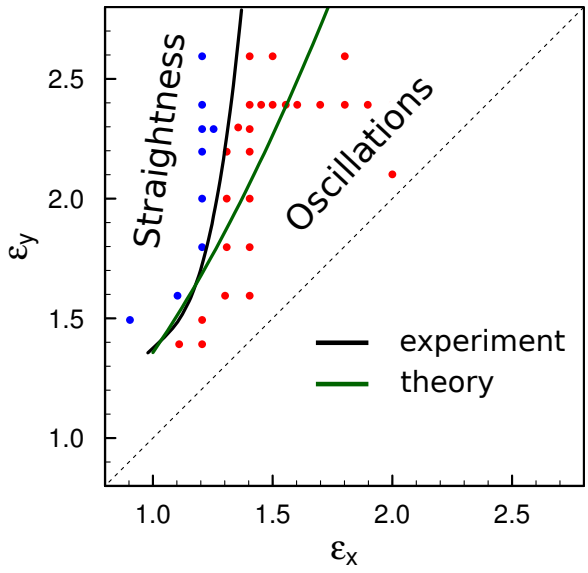

Figure 3.5: A comparison of the phase diagrams of oscillations obtained from experiment and from theory. The black line represents the phase boundary obtained from experiments and the green line represents the phase boundary predicted by the constraint of $T/K_I^0 = 2.72/\sqrt{10\text{ cm}}$ when the critical crack speed at the onset of oscillations in rubber is given by $v = 0.96c_s$. This model agrees well with the experimental results of [13] (cf. fig. 3.2).

tions is $\Lambda = 2\pi/k_c = 8.5$ cm, which agrees with the observations of [13].

3.5 Conclusion

Although linear elastic fracture mechanics provides good descriptions of single cracks moving in a straight line, it fails to provide satisfactory explanation for oscillating cracks in thin elastic films such as gels and rubber. The experimental results show that oscillating cracks in gels and rubber travel above about 90% of the shear wave speed. A theory has been proposed for the

onset of oscillation in gels, but it cannot explain the oscillations in rubber. In this project, we provide a theory able to describe the oscillating cracks in both gels and rubber and recover the experimental phase diagram for oscillating cracks in rubber. The model proposed for the onset of oscillations in gels in a somewhat simpler way than has been found before.

Here, we suggest a dimensionless force $f = -B(v) K_{II}/K_I$, which drives the rotational motion of crack. We propose a generalized equation of motion, eq. (3.10), to explain the oscillatory instability. In this model, a generalized force $\overline{f}$, which is the convolution of f and a weighting function, Φ. We use a simple weighting function $\delta(x - \ell_p)$ to describe the causality due to the finite size of nonlinear zone which is originated proposed by Bouchbinder [3]. Our theory predicts that the critical crack speed at the onset of oscillations in gels is $0.8c_s$, which agrees well with experiments and other analytic solutions. Besides, the prediction of the onset wavelength $\Lambda = 4\ell_p$ shows satisfactory agreements with the observations of the size of the fracture process zone [5].

Although the equation of motion for cracks in rubber is still unclear, this study presents a way to describe the shape of the phase diagram of oscillating cracks in rubber that requires almost no details of the equation of motion. Nevertheless, the simple time delay model is ruled out based on the constraints in $\Psi(q)$. Alternatively, an overdamped oscillation model that satisfies the constraints in $\Psi(q)$ is proposed, and this model gives satisfactory agreement with experiments.

Chapter 4

Discrete Model of Hydraulic Fracture

This chapter presents numerical work on "Physics of Hydrocarbon Recovery in Shales," which is one of the ongoing projects in the Shell-UT Unconventional Research Program. The Shell-UT Unconventional Research Program, funded by Shell Oil Co., is a collaborative program in which multiple departments from the University of Texas at Austin and Shell work jointly on solving complex problems of unconventional hydrocarbon resources.

4.1 Introduction

Shale gas is natural gas locked in tight, impermeable shale formations. In the past, it was hard to believe that shale gas could be produced commercially even though it is globally abundant (fig. 4.1). The applications of two techniques, horizontal drilling and multistage hydraulic fracturing, have greatly increased the productivity of natural gas wells. Shale gas drilling is rapidly expanding across the U.S.: in 2013, Hughes reported that [29]

"Large-scale shale-gas production was initiated in the Barnett Shale

> formation a decade ago, and it spread quickly to other areas. Five plays produce 80% of US shale gas (listed from highest to lowest output): Haynesville in Louisiana, Barnett in east Texas, Marcellus (which spans West Virginia, Pennsylvania and New York), Fayetteville in Arkansas and Woodford in Oklahoma."

Shale gas production has recently risen in the U.S.: shale gas production accounted for about 40% of U.S. gas production in 2012; it was just 2% in 2000 [29]. The shale gas boom has transformed the U.S. energy market and the country is projected to become a net exporter of natural gas in the very near future [10].

Hydraulic fracturing, or hydrofracturing, refers to a well stimulation treatment that enhances the production of oil or gas originally locked in low permeability reservoirs. This is not a brand new technology; the very first application of this technology was used to produce oil and gas in Kansas's Hugoton field in 1947 [1, 23]; since then, hydraulic fracturing has been used in more than one million oil and gas wells [28]. Horizontal drilling, a well stimulation treatment used to extend the length of horizontal wells within target formations, can greatly increase productivity. Horizontal drilling has recently overtaken traditional vertical drilling as the most common practice for drilling wells; 10% of U.S. wells were horizontal in 2004 but the number increased rapidly to 61% by 2013 [29]. The combination of horizontal drilling and hydraulic fracturing has become a standard well treatment for shale gas extraction today.

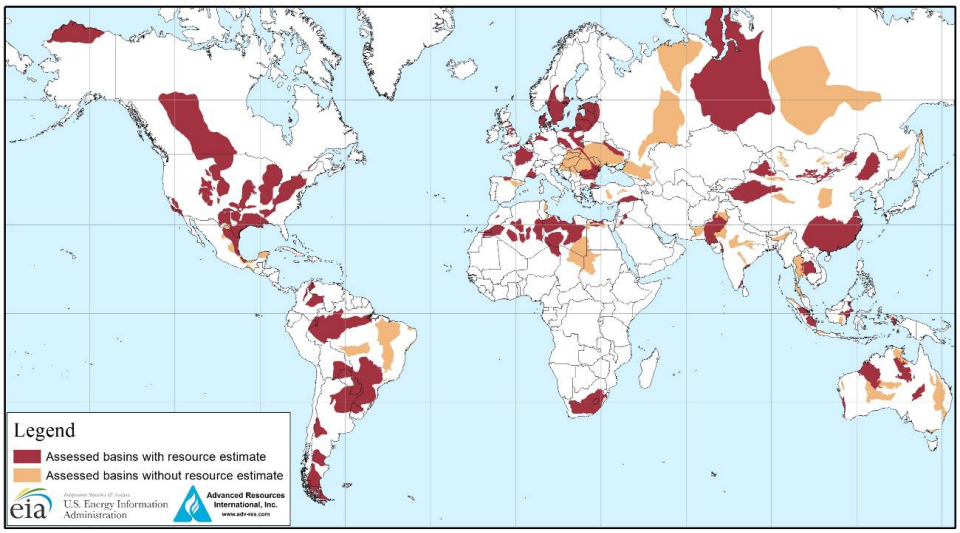

Figure 4.1: Map of shale basins with assessed shale oil and shale gas formation, as of May 2013. Source: U.S. Energy Information Administration (EIA). This map shows the most important shale reservoirs in a group of 41 nations. The map legend indicates three different colors on the map corresponding to their assessments: Red colored areas represent the location of assessed basins with shale formations and provided shale resource estimates. Tan colored area represents the location of basins that were reviewed but with no estimates yet. White colored areas indicates the locations have not been assessed.

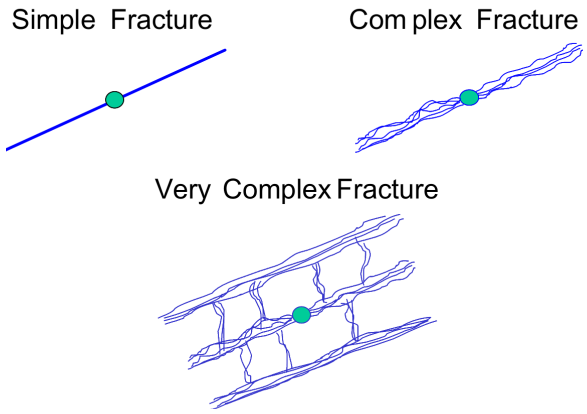

Figure 4.2: Fracture complexity. Source: Fisher et al. (2002) [17].

The development of simple theoretical models of hydraulic fracturing started in the 1950s. Two classical simplified models, the PKN model and the KGD model, provide relatively simple analytical solutions for single planar pressure-driven fracture problems [20, 33, 48, 52]. Nevertheless, the widely-held assumption of a single planar hydraulic fracture for the past 60 years has been challenged by recent studies [12, 17, 21, 50]. Figure 4.2 shows the possible patterns of hydraulic fractures, and these pasterns can be complex. Characterizing the connectivity of these complex fracture networks is a key factor in predicting well performance, but, unfortunately, the existing single-planar-fracture models are not able to model these complex fracture networks.

The main aim of this project is to investigate these complex patterns of hydraulic fractures by means of a discrete model which can adequately simulate the formation and evolution of hydraulic fractures.

4.1.1 Background and challenges

This section presents an overview of hydraulic fracturing and the challenges in modeling hydraulic fracturing.

Hydraulic fractures, driven by internal fluid pressure, represent a very special case of fracture mechanics. It is a complex coupled system: the basic ingredients of hydraulic fracturing contain elastic deformations of rock, fracture formations of rock, a viscous flow within fractures, and rock-fluid interactions.

Figure 4.3 shows a typical hydraulic fracturing process. A well is drilled vertically until the drilling reaches target shale formations, usually 2-3 kilometers below the earth's surface. A concrete casing is inserted to stabilize the wall and prevent any leakage of fracturing fluid contaminating aquifers. Then the drillbit turns at a 90 degree angle and continues to drill into the shale formations horizontally. The horizontal well may extend approximately 1500 meters. After the drilling is done, a perforation gun is sent down to the horizontal section of the well and fired to generate a series of small initial cracks on the wellbore walls before the hydrofracturing. Once the perforations are completed, high-pressure fracturing fluids are injected into the reservoir to fracture shales. Fracturing fluids are generally water-based fluid mixed with a number of chemical additives and fracturing sand or other proppants. During hydraulic fracturing, the fluids can either go into wells or leak away into reservoir pore space. Once the hydraulic pressure is released from the well, the fractures are held open by proppants, which enable oil or gas originally trapped in the formations to migrate from the reservoir to wellbore and then

up to the surface.

Shale is neither isotropic nor homogeneous because it is highly layered and sometimes naturally fractured. Neglecting these effects may lead to well drilling failures. Including the details of the randomness in shales as much as possible is important for this problem; however, it will bring more challenges.

Additional challenge is caused by the high computational demand associated with the resolution required in time and spatial scales when modeling hydraulic fracturing. Hydraulic fracturing is a multiscale system that exhibits a wide of range of length scales and time scales. The largest scale of hydraulic fracturing is the reservoir scale, which is on the order of kilometers; the smallest fracture width important for hydraulic fracturing can be on the order of micrometers. The largest time scale is the injection time, which is on the order of hours [58] and the smallest timescale is the time needed for fluid pressure to equilibrate locally within a small region of a fracture filled with fluid, which is typically $10^{-7} - 10^{-5}$ s (the order of magnitude estimates will be discussed in more detail in the next section). It turns out that this system encompasses a 10^6 range in spatial scales and a range of about 10^{10} in time scales. It is crucial for this research to develop a relevant model which can cover the time and spatial scales of interest while keeping computational costs low.

The study considers a simple case where hydraulic fractures are driven by high-pressure water in an impermeable elastic medium without any leakages. A numerical model was developed to overcome the challenges mentioned above; it provides three major advantages: accommodating arbitrary geome-

tries, resolving kilometer-scale wells, and adding the features of anisotropy and heterogeneity without difficulty.

4.1.2 Order of magnitude estimates

This section presents order of magnitude estimates for a hydraulic fracturing system, which includes a fluid component and a solid component.

An essential observation that underlies studies of engineering hydraulic fracture is that the smallest timescale in the problem is the time needed for fluid pressure to equilibrate locally within a small region of a fracture filled with highly pressurized fluid. The characteristic width of a hydraulic fracture is 1 mm (with the possibility of factors of ten larger and smaller) [52]. Since the speed of sound in water is of 1500 m/s, the characteristic time for pressure equilibration is $10^{-7} - 10^{-5}$ s.

Although the speed of sound in rock is several times greater than in water, when choosing one meter as the characteristic spacing within the rock in lumped elastic models for the rock, the larger spatial scale means that the characteristic time for rock to move during dynamic fracture will be 10^{-3} s. This is not a huge separation of time scales, but it appears to be the best starting point. It leads to great gains in numerical efficiency, since taking pressure equilibration of the fluid to be fast means there is no need to model the fluid in detail.

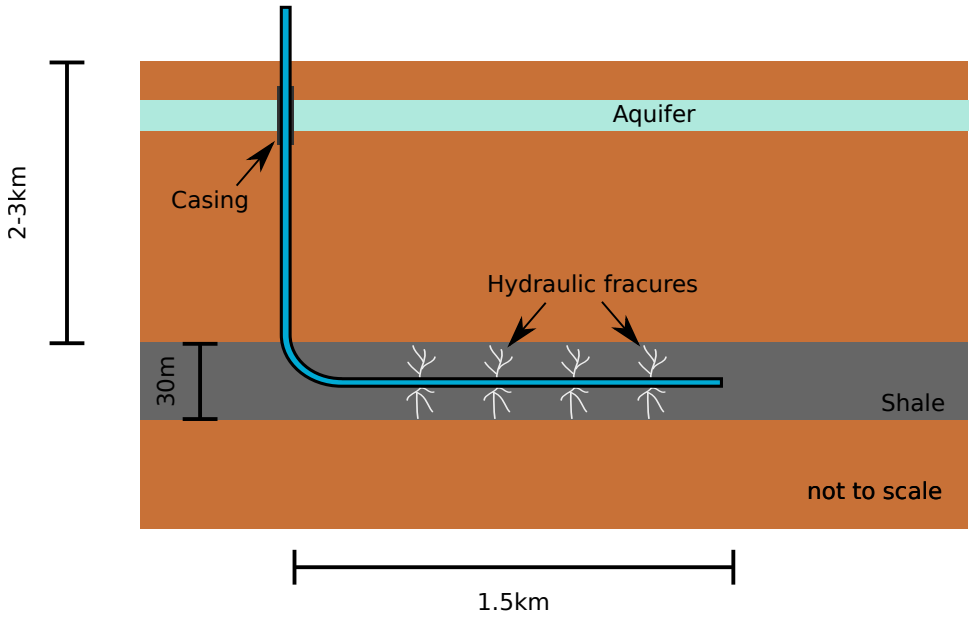

Figure 4.3: Schematic of hydraulic fracturing process. Hydraulic fracturing is a technology to unlock the natural gas trapped within impermeable rocks, such as shales or clays. A well is drilled vertically until the drilling reaches target shale formations, usually 2-3 kilometers below the earth's surface. A steel casing that is cemented is used to line the wellbore, stabilize the wall and prevent any leakage of fracturing fluid contaminating aquifers. Then the drillbit turns at a 90 degree angle and continues to drill into the shale formations horizontally. The horizontal well may extend approximately 1500 meters. After the drilling is done, a perforation gun is sent down to the horizontal section of the well and fired to generate a series of small initial cracks on the wellbore walls before the hydrofracturing. After perforating, highly pressurized fracturing fluids are injected into the reservoir to fracture shales. Typically, fracturing fluid is made up of approximately 90% water, 9.5% sand and 0.5% chemical additives.

4.2 Fluid transport

The equation incorporating the idea of rapid pressure equilibration of a fluid is Reynolds' lubrication approximation [56]. Consider a steady flow in a channel of width w (fig. 4.4). The fluid is assumed to have adopted a laminar flow profile and is treated as incompressible, meaning that any change in the amount of fluid in a small region must correspond to an increasing width of the channel, with a corresponding rise in pressure.

Let $\vec{v} = (v_x, v_y, v_z)$ represent the fluid velocity. The fluid velocity vanishes at the top and bottom boundaries to leading order, so take

$$\vec{v} = (v_x, v_y, v_z) \approx \vec{u} f(z) + \hat{z} v_z = \vec{u} \frac{z}{w} \left(1 - \frac{z}{w}\right) + \hat{z} v_z. \tag{4.1}$$

where $\vec{u} = (v_x, v_y)$ has only x and y components. From the incompressibility of the flow, $\vec{\nabla} \cdot \vec{v} = 0$, we have

$$\frac{\partial v_z}{\partial z} = -\vec{\nabla} \cdot [\vec{u} f(z)]\,. \tag{4.2}$$

Let $w(x, y)$ give the local width of the channel. Integrate in z from 0 to w. Then

$$v_z(w) - v_z(0) = \frac{\partial w}{\partial t} = -\vec{\nabla} \cdot \left(\frac{w}{6} \vec{u}\right). \tag{4.3}$$

From the Navier-Stokes equation for nearly steady flow,

$$-\vec{\nabla} P + \mu \nabla^2 \vec{v} = 0, \tag{4.4}$$

where P is fluid pressure, and μ is the viscosity of fluid. The fluid used in hydraulic fracturing is typically water-based; it is comprised of approximately 90% water, 9.5% sand and 0.5% chemical additives. To simplify this problem, here we use a fracturing fluid viscosity that has the same value as the water viscosity, i.e., $\mu = 10^{-3}$ Pa·s.

Since the largest gradients are along z to leading order

$$-\vec{\nabla}P = 2\mu\frac{\vec{u}}{w^2} \Rightarrow \vec{u} = -\frac{w^2}{2\mu}\vec{\nabla}P. \tag{4.5}$$

Substituting eq. (4.5) into eq. (4.3) gives

$$\frac{\partial w}{\partial t} = \vec{\nabla}\cdot\left(\frac{w^3}{12\mu}\vec{\nabla}P\right). \tag{4.6}$$

For orders of magnitude, take $\mu = 10^{-3}$ Pa·s, the characteristic channel width w of 1 mm and consider pressures on the order of 10 MPa that change on the scale of 10 meters. From eq. (4.6), the rate of change in the fracture width over time is $\partial w/\partial t \sim \left(10^{-3}\text{m}\right)^3/\left(10^{-3}\text{Pa·s}\right)\left(10\text{MPa}\right)/\left(10\text{m}\right)^2 \sim 0.1\text{m/s}$. Comparing this velocity with the characteristic channel width w of 1 mm, one finds a characteristic time of 10^{-2} s. That is, viscous flow will cause changes on the order of 1 mm in channel widths on the scale of 0.01 seconds. For channels 10 times wider, the changes will be 1000 times faster, approaching the timescale for pressure equilibration. On the other hand, if the spatial scale of pressure gradients is 100 meters rather than 10 meters that will slow

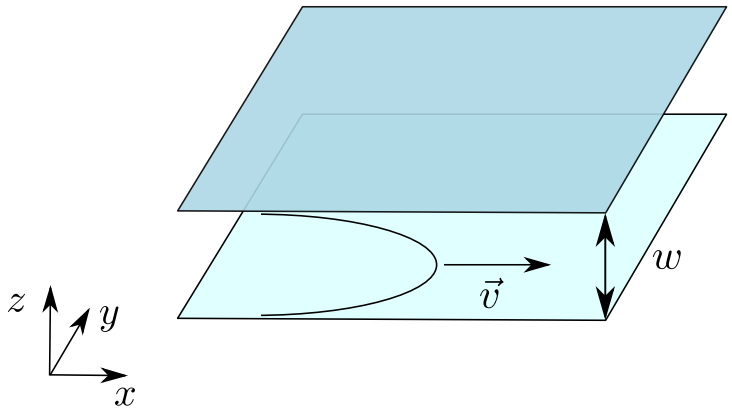

Figure 4.4: Figure showing the geometry of the lubrication approximation. The channel width w is small compared to the dimensions of the plates. The flow velocity is denoted by $\vec{v}$. The fluid is assumed to have adopted a laminar flow profile. It is assumed that the flow is incompressible and the fluid velocity vanishes at the top and bottom boundaries.

the process down by a factor of 100. Therefore the assumption of pressure equilibration embodied in the lubrication approximation, eq. (4.6), appears to stand up to examination through simple estimates.

4.2.1 Simplified models

This section presents two classical models for simple geometries, the PKN model and the KGD model , which provide insight into this problem and a benchmark for validating our numerical models as well.

The development of simple theoretical models of hydraulic fracturing started in the 1950s. Based on the assumptions of the fracture geometries, there are two limiting cases, the PKN model [48, 52] and the KGD model [20, 33], as shown in fig. 4.5. In these models, the fracture height H is assumed

constant during fracturing along the horizontal direction (x-direction); only the fracture width w and the fracture length L are allowed to change. The PKN model assumes that the fracture opens and closes in the vertical direction (y-direction), and fluid pressure P has a chance to equilibrate and does not depend upon y. The KGD model assumes that the fracture is uniform in the y direction.

Simple relations between the crack width w and fluid pressure P can be found in these models based on the following assumptions. Let σ_c describe the total earth stress perpendicular to the plane of the fracture, i.e., the local minimum confining stress, let P describe the fluid pressure, and define $P_d = P - \sigma_c$. Suppose one applies pressure P in the interior of a very long thin deeply buried fracture. Then, if the gradients in pressure are not too large, one would expect the fracture width would depend on P_d in a fracture region of length L and height H, Young's modulus Y and Poisson's ratio ν. Sneddon suggests that the crack width w and P_d are related through [60]

$$w(x,t) = \gamma P_d(x,t), \tag{4.7}$$

where $\gamma = 2H(1-\nu^2)/Y$ for the PKN model and $\gamma = 2L(t)(1-\nu^2)/Y$ for the KGD model.

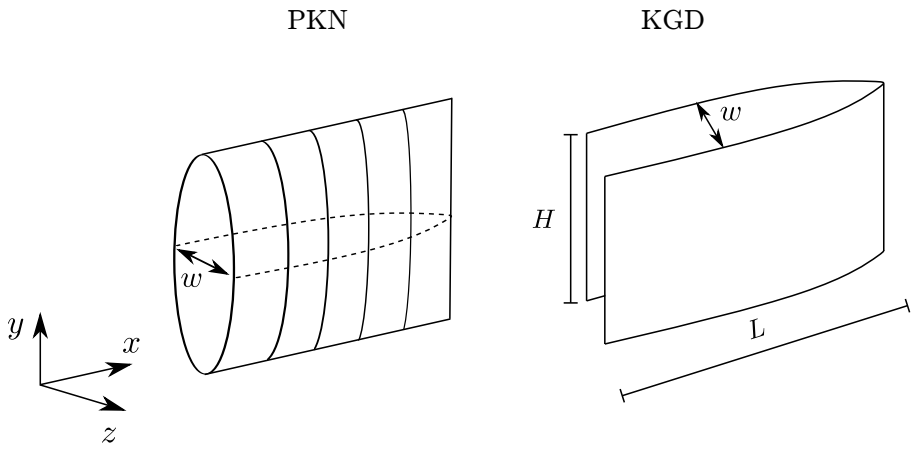

Figure 4.5: Geometries of two hydraulic fracture model configurations. The fracture height H is assumed constant during fracturing along the x-direction; only the fracture width w and the fracture length L are allowed to change. In the PKN model, the fracture opens and closes in the y-direction; fluid pressure P has a chance to equilibrate and does not depend upon y. In the KGD model, the fracture is uniform in the y direction. A vertical fracture propagates in two wings (180° apart and identical in shape) from a wellbore. This figure only shows the wings of the fractures moving in the positive x-direction.

4.2.2 Scaling laws in the KGD model

This section presents the scaling laws in the KGD model. Take the assumptions for the KGD geometry and insert eq. (4.7) into the volume integral of eq. (4.6). A vertical fracture propagates in two wings (180° apart and identical in shape) from a wellbore. Let the origin of coordinates be located at the center of the two-wing fracture. Without loss of generality, we only consider the wing of the fracture moving in the positive x-direction in the following discussion, i.e., $x \in (0, L)$.

Assuming a nearly time-independent solution, varying along x, with constant injection rate Q, with fracture height H, we have

$$-\frac{Q}{H} = \frac{\gamma^3 P_d^3}{12\mu}\frac{\partial P}{\partial x}. \tag{4.8}$$

Solving eq. (4.8) by imposing the boundary condition $P_d\,(x = L) = 0$, or $P\,(x = L) = \sigma_c$, we obtain

$$P\,(x) = \sigma_c + \left[\frac{48 Q\mu(L - x)}{H\gamma^3}\right]^{1/4}. \tag{4.9}$$

Insert eq. (4.9) into eq. (4.7) to obtain the crack width

$$w\,(x) = \left[\frac{48\gamma Q\mu(L - x)}{H}\right]^{1/4}. \tag{4.10}$$

If we take L to be changing slowly then the volume of the crack is

$$\begin{aligned} V &= \int_0^L Hw\left(x\right) dx \\ &= \frac{8}{5} H^{3/4} \left[\frac{6(1-\nu^2)}{Y} Q\mu\right]^{1/4} L^{3/2} \end{aligned} \tag{4.11}$$

Assuming no fluid loss into the reservoir, the total volume of water injected into the system at time t is

$$V = Qt. \tag{4.12}$$

From eq. (4.11) and eq. (4.12), the fracture length

$$L\left(t\right) = C_1 \left(\frac{Q}{H}\right)^{1/2} t^{2/3}, \tag{4.13}$$

where

$$C_1 = \left(\frac{5}{8}\right)^{2/3} \left[\frac{Y}{6(1-\nu^2)\mu}\right]^{1/6}.$$

Insert eq. (4.13) into eq. (4.10). The crack width at $x = 0$ can be written as

$$w\left(t, x=0\right) = C_2 \left(\frac{Q}{H}\right)^{1/2} t^{1/3}, \tag{4.14}$$

where

$$C_2 = \left[\frac{150(1-\nu^2)\mu}{Y}\right]^{1/6}.$$

Insert eq. (4.13) into eq. (4.9). We have

$$P\left(t, x=0\right) = \sigma_c + C_3 t^{-1/3}, \tag{4.15}$$

where

$$C_3 = 2\left(\frac{6}{5}\right)^{1/3} \mu^{1/3} \left[\frac{Y}{(1-\nu^2)}\right]^{2/3}.$$

As a fracture grows in size during hydraulic fracturing, its fracture length L scales as the two-third root of time in eq. (4.13); its fracture width w scales as the third root of time in eq. (4.14). The pressure P falls off at the base of the crack as the third root of time in eq. (4.15). The height of the crack H should appear only in the combination Q/H, since the physical conditions are unchanged so long as the injection rate Q and the crack height H increase simultaneously by the same factor. Equation (4.15) shows that the scaling law of fluid pressure P depends upon Young's modulus Y, Poisson's ratio ν and the viscosity of fluid μ but not upon the combination Q/H.

4.3 Numerical Methodology

Our model has systems that interact with each other: discrete mass points that obey rules for elasticity and fracture, and discrete channel and fluid variables that describe the flow of fluid in a network of fractures. For the moment we specialize to a square lattice: generalization to other lattices creates some technical challenges we have not yet solved. This model fully

contains two-dimensional linear elasticity plus fracture mechanics, plus fluid flow.

The model is sketched in fig. 4.6. There is a set of mass points arranged on a square lattice with a lattice spacing a and each mass point represents a lump of rock of volume a^3. These mass points will interact with nearest neighbors only and have a force law that is a general linear functional of relative displacements of neighbors. Therefore although the points are defined on a square lattice, the lattice can have any desired shear resistance. A one meter spacing is chosen for the following reasons. First, from the estimates in Section 4.1.2, this choice means that the time scale for communication between mass points is slower than the time needed for equilibration of pressure within millimeter-scale channels. Second there will be a fracture criterion based on separation of mass points. The physical separation of the mass points will be understood to be on the order of a meter, and the fracture criterion will correspond to motions on the order of a small distance $\delta \ll 1$ mm calculated below.

Fracture criteria are easy to model in discrete frameworks; for example, one can say that fracture occurs when the spacing between two mass points passes a critical threshold. The rock medium is assumed to be an ideal brittle material, Young's modulus for rock is typically 50 GPa and the fracture energy for shales, Γ, is on the order of 100 J/m^2 [61]. For a spring of length $a = 1$ m, the spring constant is roughly $k = Ya$ =50×10^9 J/m^2. The concept of Griffith failure is used here: the Griffith criterion, $\Gamma a^2 = k\delta^2/2$, yields the extension at

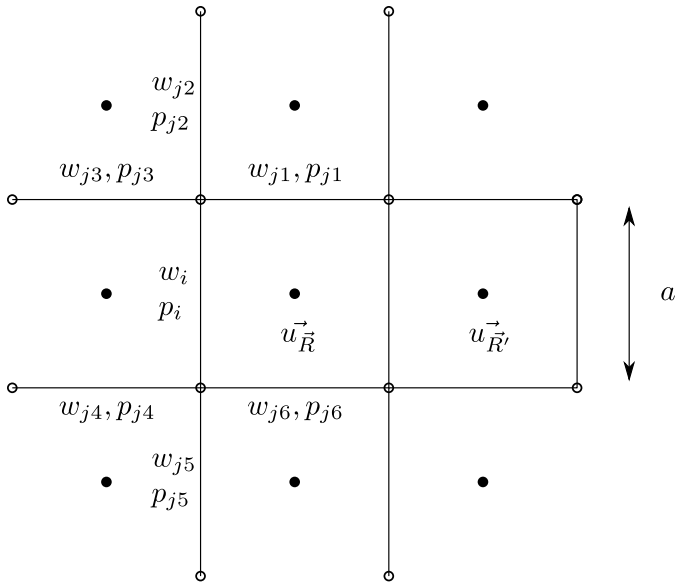

Figure 4.6: Geometry of lattice model of hydraulic fracture. Here, $\vec{R}$ and $\vec{R}'$ represent two neighbor mass points, w_i represents the channel width of channel i and p_i represents the pressure in the channel segment i. Let j_k represent the kth channel connecting to channel i, where k is a positive integer up to six. The lattice spacing a is chosen equal to one meter in our current model.

failure of order $\delta = \sqrt{2\Gamma a/Y}$ which comes out to 6×10^{-5} m. This is 0.06 mm, which is on the order of the smallest fracture width that can be important for hydraulic fracture.

4.3.1 Modeling Hydraulic fracturing Process

Here is how the model goes. So long as all the bonds on a mass point are unbroken, it evolves according to the dynamics of elasticity. As soon as a bond breaks between two mass points, a channel w between the two mass points is activated, and the distance between the mass points on either side is

now controlled by eq. (4.6) rather than elasticity. The pressure in any channel segment is given by the average normal force of mass points on either side.

To be more specific, referring to fig. 4.6, the force on a lumped mass point $\vec{R}$ is given by

$$\vec{F}_{\vec{R}} = \sum_{\vec{R}' \in nn(\vec{R})} \begin{cases} (k_\parallel - k_\perp)(\vec{\delta u}_{\vec{R},\vec{R}'} \cdot \hat{\Delta}_{\vec{R},\vec{R}'}) \cdot \hat{\Delta}_{\vec{R},\vec{R}'} + k_\perp \vec{\delta u}_{\vec{R},\vec{R}'} & \text{if } |\delta \vec{u}_{\vec{R},\vec{R}'} < \delta| \\ ap_{\vec{R},\vec{R}'} \hat{\Delta}_{\vec{R}\vec{R}'} & \text{else} \end{cases} \tag{4.16}$$

Here $\vec{\Delta}_{\vec{R},\vec{R}'} \equiv \vec{u}^0_{\vec{R}'} - \vec{u}^0_{\vec{R}}$ is the vector difference between neighbors of the undistorted lattice, $\vec{\delta u}_{\vec{R},\vec{R}'} \equiv \vec{u}_{\vec{R}'} - \vec{u}_{\vec{R}} - \vec{\Delta}_{\vec{R},\vec{R}'}$ is the relative displacement of the two mass points from their original locations and $\hat{\Delta}_{\vec{R},\vec{R}'} \equiv \vec{\Delta}_{\vec{R},\vec{R}'} / \left| \vec{\Delta}_{\vec{R},\vec{R}'} \right|$. The pressure $p_{\vec{R},\vec{R}'}$ is only present when the bond between two neighbors has snapped. The value of the pressure is determined by the fluid model, which follows. In cases where this pressure is present, the other terms in eq. (4.16) vanish between $\vec{R}$ and $\vec{R}'$. Poisson's ratio for shales typically ranges from about 0.05 to 0.3 [22, 52]. The constants $k_\parallel$ and $k_\perp$ make it possible to describe solids with arbitrary Poisson's ratio. On the square lattice, for propagation along a symmetry axis,

$$c_d^2 = \frac{k_\parallel}{m}; \quad c_t^2 = \frac{k_\perp}{m}. \tag{4.17}$$

Here c_d and c_s represent the dilatational wave speed and the shear wave speed of the solid medium, respectively. Poisson's ratio ν are related with the speeds

of sound through the following equation

$$\nu = \frac{c_d^2 - 2c_s^2}{2\left(c_d^2 - c_s^2\right)}. \tag{4.18}$$

The elastic force drops to zero when $\delta\vec{u}_{\vec{R},\vec{R}'} > \delta$. As soon as this happens, $w_{\vec{R},\vec{R}'}$ is set to an initial value of δ.

The fluid portion of the model is described by the following discrete system. Referring again to fig. 4.6, let j be all the channels that connect to channel i. There could be up to six of them, depending upon how many of them have broken open. Let w_i be the width of channel i and let v_{ij} be the rate at which fluid flows from channel j into channel i. Then

$$\frac{\partial w_i}{\partial t} = \frac{1}{a} \sum_{j \in \mathrm{nn}(i)} v_{ij} w_{>}. \tag{4.19}$$

$$v_{ij} = \frac{w_{>}^2}{12\mu} \frac{p_j - p_i}{a}; \quad w_{>} = w_j \text{ if } p_j > p_i, \text{ else } w_i. \tag{4.20}$$

The reason to use $w_{>}$ is that as is usual in convective problems one must use variables that correspond to the upstream portion of a flow in computing downstream properties. The pressures in channel segments i and j are p_i and p_j, respectively. If the mass points perpendicular to segment i are $\vec{R}$ and $\vec{R}'$ then p_i is $p_{\vec{R},\vec{R}'}$.

The model proceeds in time by using Newton's laws for the mass points described by eq. (4.16) employing the Verlet algorithm. Once the bond be-

tween two mass points breaks, the channel variable between them becomes active, and the channel is controlled by eqs. (4.19) and (4.20). If a vertical bond has broken, then the vertical positions of $\vec{u}_{\vec{R}}$ and $\vec{u}_{\vec{R}'}$ are adjusted so that the sum of vertical forces on them vanishes, and the vertical force on each of them divided by the segment width a is identified as the pressure. An analogous procedure applies to horizontal bonds.

The energy dissipation in the solid medium is described by a simple Kelvin model (see Sec. 1.2 for more details). Thus, the dissipative force on a lumped mass point $\vec{R}$ is given by

$$\vec{F}_{\vec{R}} = \sum_{\vec{R}' \in nn\left(\vec{R}\right)} \beta \left(\frac{\partial \vec{u}_{\vec{R}'}}{\partial t} - \frac{\partial \vec{u}_{\vec{R}}}{\partial t} \right) \theta \left(\delta - \delta \vec{u}_{\vec{R},\vec{R}'} \right), \tag{4.21}$$

where θ is the Heaviside step function. In this study, the dissipation parameter is set to $\beta = 5$ J·s/m^2, which was obtained from a simulation designed to reproduce the conditions of the KGD model.

4.4 Model validation

The current model has been validated via a comparison with the KGD model. Figure 4.7 shows the setup with the origin of coordinates at the center of the system. The system size is set to 50 m × 20 m × 30 m (Length × Width × Height). The fracture is uniform in the y-direction, and fracture height H is assumed constant in hydraulic fracturing. Here, water is injected into the

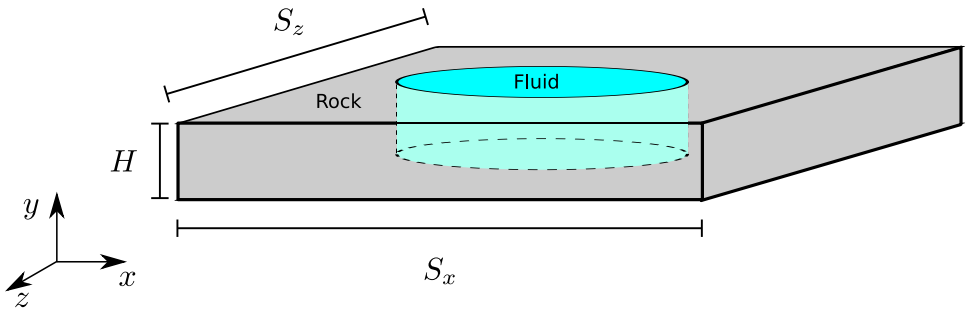

Figure 4.7: Figure of a single hydraulic fracture in a three dimensional box with length S_x, width S_z and height H. The fracture height H is assumed constant at all times. The origin of coordinates is at the center of the system.

system through a line source along the y-axis over the height of the system. The parameter values used in this case are $\Gamma = 100$ J/m^2, $Y = 50$ GPa, $\nu = 0.25$, $\mu = 10^{-3}$ Pa·s and $Q = 0.03$ m^3/s (equivalent to 11.32 bbl/min). Here, 1 m^3/s is equivalent to 377.39 bbl/min. According to eq. (4.15), pressure at the base of a crack should fall off in time as

$$P(t) = \sigma_c + C_3 t^{-1/3}, \tag{4.22}$$

where $C_3 = 3.01$ MPa·s$^{1/3}$. The agreement between numerical calculations and the KGD model is good, as shown in fig. 4.8.

4.5 Results and discussion

A series of pilot simulations was systematically tested for complex geometries under more realistic operation conditions, including a flexible boundary condition, randomness in shales and perforations. The current study con-

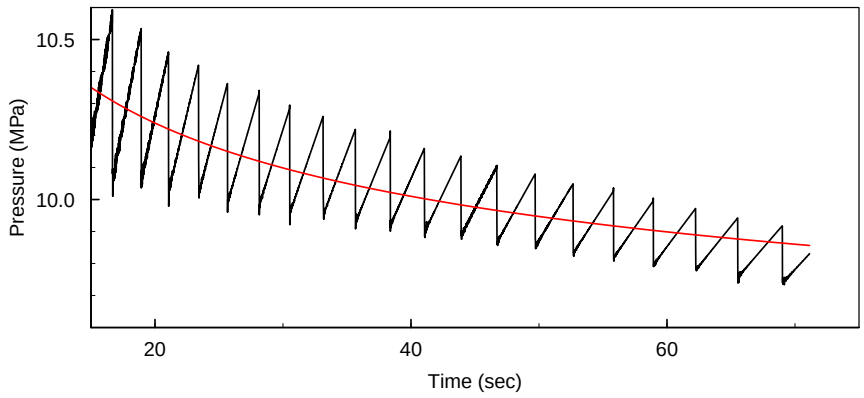

Figure 4.8: Pressure versus time for a simulation designed to reproduce the conditions of the KGD model. The black line represents the numerical results and the red line is fitted to the data by using eq. (4.22), with the parameter $\sigma_c = 9.13$ MPa. The oscillation in the data is primarily due to the flow of fluids into new open channels during hydraulic fracturing. The system size is 50 m $\times$ 20 m $\times$ 30 m (Length $\times$ Width $\times$ Height) and the injection rate is Q=0.03 m^3/s. The agreement between numerical calculations and theory is good.

siders pseudo-3D fracture propagation problems where all fractures have the same height as the system and all fractures are uniform along the height direction.

4.5.1 Boundary conditions

In first simulations, the boundaries of the fracturing system were assumed rigid. Neglecting the movements of the boundaries simplifies this problem; it provides a good starting to study hydraulic fractures, but the rigid boundary condition is not an appropriate representation of the real situations when studying hydraulic fracturing at high injection rates. This is not physical because the confining pressure increases without bound with the increasing water in the system; either the shape of the system needs to change or a portion of the water in the system needs to disappear in responsible for it. The former is considered here and the latter will be left for future work.

Thus, a flexible boundary condition is designed for systems with high injection rates. This boundary condition is described as follows. Consider a fracturing system surrounded by a less stiff outer solid medium with rigid boundaries, as shown in fig. 4.9. The initial stresses on the fracture boundaries is estimated to be the earth stress. This setup allows the fracturing system to change its shape to equilibrate the applied stresses on its boundaries during hydraulic fracturing. In the following discussion, the outer medium is set to 10 times less stiff than the inner medium.

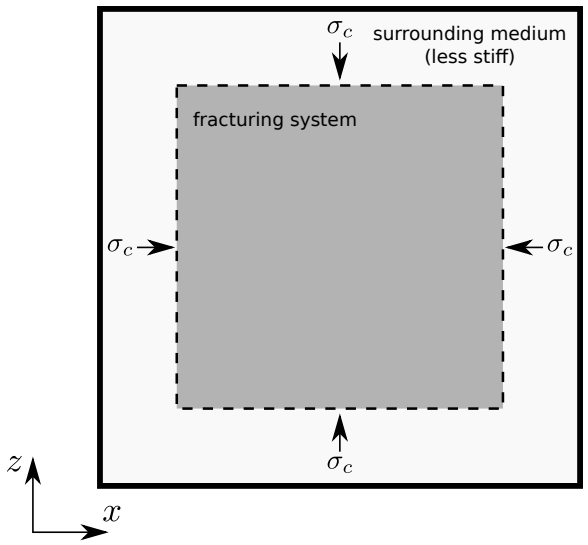

Figure 4.9: Figure of a fracturing system embedded in a less stiff solid medium (top view). The initial applied stresses on the fracturing system walls are set to σ_c, the total earth stress applied to this system. This setup allows the fracturing system to change its shape to equilibrate the applied stresses on its boundaries easily.

A series of test runs was designed to examine these two types of boundary conditions. The system size was set to 30 m $\times$ 50 m $\times$ 30 m (Length $\times$ Width $\times$ Height). The parameter values used in this case are $\Gamma = 100$ J/m^2, $Y = 50$ GPa, $\nu = 0.25$ and $\mu = 10^{-3}$ Pa·s. The injection rate Q varied from 0.03 m^3/s to 0.3 m^3/s. A comparison of the first-two minute numerical results with the KGD model suggests that when $Q < 0.05$ m^3/s, there is no significant difference between using these two types of boundary conditions; when $Q > 0.05$ m^3/s, the flexible boundary condition is a more appropriate representation of real situations.

4.5.2 Randomness in shales

Shale is neither isotropic nor homogeneous due to the alignment of clays and the presence of microcracks. Including all the details of the randomness in shales may greatly complicate this model. The present work only considers a simple case where fracture energy of rocks is normally distributed with a mean of 100 J/m^2 and a standard deviation of 0.1; Young's modulus of rocks is normally distributed with a mean of 50 GPa and a standard deviation of 0.1.

4.5.3 Perforations

Perforation is a technique used to generate a series of small initial cracks on the wellbore walls before hydraulic fracturing. These small pathways provide easier access for fracturing fluid into the reservoir at the beginning of the hydraulic fracturing. The spacing, length and angle of perforations may affect the performance of hydraulic fracturing. In the current study, the perforation angle is set to a right angle, the length of perforations is six meters and the spacing of perforations varies from two meters to tens of meters.

4.5.4 Multi-fracture interference study

A study was designed to investigate multi-fracture interference in a perforated medium. In this study, an array of seed cracks of length six meters is inserted into the system initially. The system size is set to 30 m $\times$ 50 m $\times$ 30

m (Length × Width × Height). All the fractures are uniform in the y direction and have the same height as the system. Take $\nu = 0.25$ and $\mu = 10^{-3}$ Pa·s. Let the origin of coordinates be located at the center of the system. Water is injected into the system through a line source along the the y-axis over the height of the system at $Q = 0.27$ m^3/s. The fracture energy of rocks is normally distributed with a mean of 100 J/m^2 and a standard deviation of 0.1; Young's modulus of rocks is normally distributed with a mean of 50 GPa and a standard deviation of 0.1. The flexible boundary condition is used and the outer medium is 10 times less stiff than the inner medium. The initial seed crack numbers varies from two to ten.

Figure 4.10 shows that a complex fracture network was observed after one minute of water injection in a simulation with two initial seed cracks. More complex fracture networks were observed after 80 seconds of water injection in a simulation with four initial seed cracks, as shown in fig. 4.11. When the seed cracks number is more than six, only about two thirds of seed cracks advanced. The results also show that the exterior seed cracks grew, branched and formed complex fracture networks; the interior seed cracks were more likely to retain their original sizes and shapes.

In general, the more initial seed cracks were inserted, the more complex fracture networks were observed in the study. This implies that perforation may increase the complexity of fracture networks. Nevertheless, not all seed cracks can successfully advance and form complex patterns due to the competition between neighboring fractures. When parallel fractures advancing

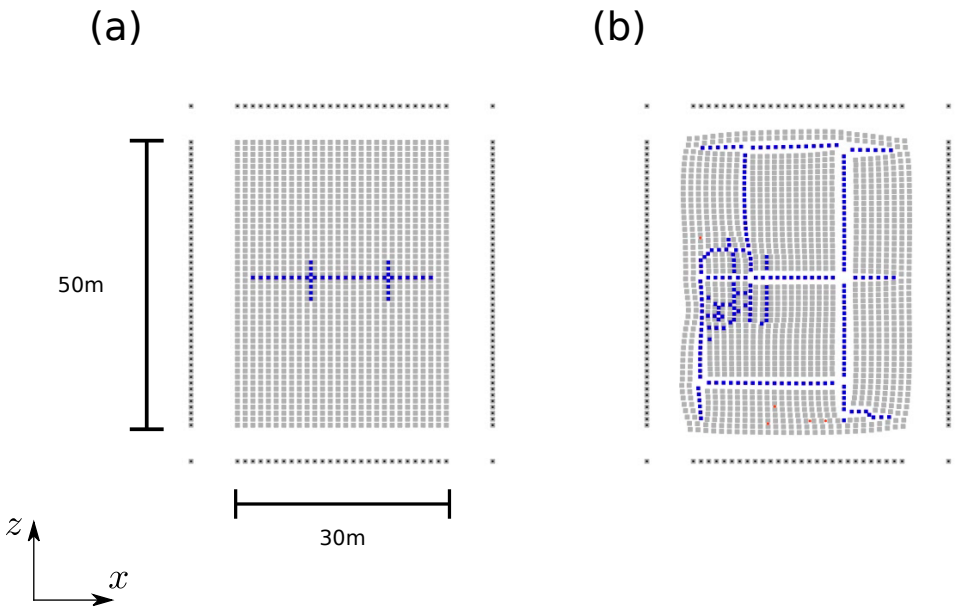

Figure 4.10: Top view of a multi-fractures interference study from a small-scale pseudo-3D simulation of region 30 m × 50 m × 30 m (Length × Width × Height) under a flexible boundary condition. (a) Two initial short seed cracks were inserted initially. (b) A complex fracture network was observed around the left seed crack after 60 seconds of water injection. The injection rate is Q =0.27 m^3/s (equivalent to 100 bbl/min). The displacement magnification factor is 1000. Cells occupied by water are colored blue, and fractured rock is colored red. The origin of coordinates is at the center of the system.

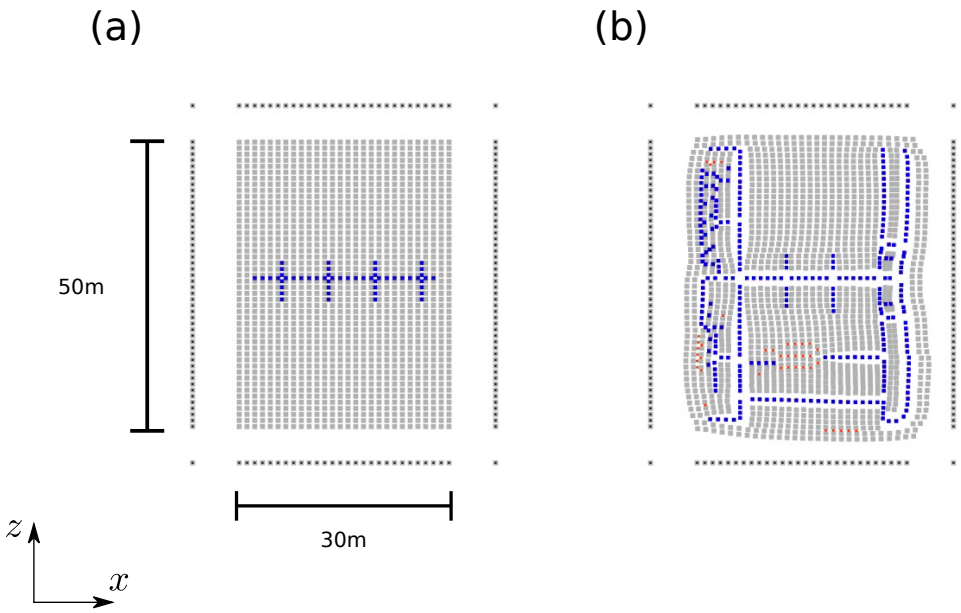

Figure 4.11: Top view of a multi-fractures interference study from a small-scale pseudo-3D simulation of region 30 m × 50 m × 30 m (Length × Width × Height) under a flexible boundary condition. (a) Four initial short seed cracks were inserted initially. (b) Complex fracture networks were observed in the regions around the leftmost and rightmost seed cracks after 80 seconds of water injection. Not all seed cracks advanced: the two exterior seed cracks grew, branched and formed complex fracture networks; the two interior seed cracks retained almost theirs original sizes and shapes. The injection rate is Q =0.27 m^3/s (equivalent to 100 bbl/min). The displacement magnification factor is 1000. Cells occupied by water are colored blue, and fractured rock is colored red. The origin of coordinates is at the center of the system.

under compression, the growth of one fracture will reduce the growth rates of its neighboring fractures. In this study, because the exterior seed cracks have fewer competitors, they can grow faster than the interior seed cracks, even though these interior seed cracks are closer to the injection source.

4.6 Computational limitations

The biggest limitation of the model is its computation efficiency. The current code uses OpenMP to speed up operations, but this method depends upon shared memory architecture and thus cannot take advantage of large parallel machines nearly as effectively as a code that uses message passing and MPI. A fully 3D kilometer-scale simulation costs about one hundred thousand hours on a desktop workstation running Linux (Fedora release 17, 32-bit) with an Intel Core i7 930@ 2.80 GHz 8-core processor. Due to the high computational demand, all the performed tests in this study were limited to pseudo-3D simulations on the scales of tens of meters in length. A parallel version of the simulation code is needed to run efficiently on parallel computers to reach the reservoir scale simulations. The memory structures in our current code were modeled on the structures in LAMMPS, an open-source parallel molecular dynamics program. It is possible to transfer this code to LAMMPS and inherit the ability to run on a massively parallel machine, but that will be left for future work.

4.7 Conclusion

Hydraulic fracturing is a common well treatment in which fluids are injected into reservoirs under high pressure to generate fractures in reservoirs. More and more evidence suggests that hydraulic fractures can be complex, but the physical mechanisms responsible for the formation of complex fracture networks are still poorly understood. In this study, a lattice-based model was developed to investigate the complexity of fracture networks. This model can provide three major advantages: it can accommodate arbitrary geometries, it can reasonably resolve kilometer-scale wells, and it adds the features of anisotropy and heterogeneity without difficulty. A set of pilot tests has been tested for complex geometries under realistic operation conditions, including flexible boundary conditions, randomness in elastic properties and perforations. The simulation results confirm that perforation is likely to increase the complexity of fracture networks; the results also suggest that the interference between neighboring fractures is key to fracture network formations. Overall, these pilot tests demonstrate the present model's ability to simulate hydraulic fracturing under a variety of operation conditions.

The continuations of this study includes an investigation of the relation between perforation angles and the complexity of hydraulic fracture networks and a qualitative analysis of the fracture complexity. The current model is built on a square lattice; the model may be improved by using other lattice structures and that will be left for future work as well. A parallel version of the simulation code will be needed to run efficiently on parallel computers to

reach the reservoir scale simulations.

Chapter 5

Conclusion

This chapter summarizes the dissertation and provides directions for future research.

5.1 Scaling of crack propagation in rubber sheets

This study investigates subsonic and supersonic cracks in rubber. Rubber is used in this study because it can suppress micro-branching instability and allows cracks to travel faster than the shear wave speed, which was a long-believed upper limit of crack speed. Based on a supersonic rupture theory developed for cracks in rubber, there exist two different scaling regimes for crack speeds: speeds of supersonic cracks are independent of system size if strain is held constant while speeds of subsonic cracks whose speed are independent of system size if energy density is held constant. The main purpose of this study is to examine this theory with experiments and numerical simulations.

Experiments in rubber were conducted at 85 °C to reduce the strain crystallization. In experiments, both subsonic cracks and supersonic cracks

were observed and the transition between subsonic and supersonic cracks was studied. A numerical model based on Neo-Hookean theory with Kelvin dissipation and a new rule for increasing toughness was developed. Calibration experiments were performed to obtain the parameters needed in this model. Numerical simulations were conducted and the results show good agreement with experiment for crack speeds and particle velocity fields.

Both experiments and numerical simulations in this study support supersonic cracks and show two different scaling regimes: the speed of subsonic cracks scales with the elastic energy density while the speed of supersonic cracks scales with the extension ratio.

In this study, the simulations slightly overestimate the openings and particle velocity. These quantitative inaccuracies are likely related to the simple dissipation form and the toughening rule employed for the simulations. A promising future direction is to consider the standard linear solid model with a more general toughening rule in this model.

5.2 Theory of oscillating cracks

Linear elastic fracture mechanics provides good descriptions of single cracks moving in a straight line, but still fails to provide satisfactory explanation for oscillatory instability. Although oscillating cracks are not seen very widely, they were found in gels and rubber. The experimental results show that the critical crack speed at the onset of oscillations in gels is about 90% of

the shear wave speed; in rubber, the main experimental findings are a phase diagram for oscillations as a function of biaxial loading, and measurements of amplitude and wavelength of oscillation once the wiggling begins. A theory has been proposed for the onset of oscillation in gels, but it cannot explain the oscillations in rubber. The main goal of this study is to provide an explanation.

A generalized equation of motion is proposed in this study based on a convolution of a generalized force and a weighting function. This force is derived based on a maximum energy release rate criterion and the weighting function can include the details of the fracture process zone, which is ignored by linear elastic fracture mechanics. Due to the causality between the stress fields outside of the fracture process zone and crack tip motion, a time delay model is proposed for oscillations in gels. The theoretical predictions for the onset of oscillations show satisfactory agreements with experiments and other analytic solutions.

Although the equation of motion for cracks in rubber is not known, this study presents a way to describe the phase diagram of oscillating cracks in rubber that requires almost no knowledge of the equation of motion. However, the simple time delay model is ruled out based on this analysis. An overdamped oscillation model that satisfies the constraints and covers the phase diagram is proposed is proposed, and it gives agreeable results with experiments.

In sum, this study provides a theory able to describe the oscillating cracks in both rubber and gels and recover the experimental phase diagram for oscillating cracks in rubber. The theory that recovers the onset of oscillations

in gels in a somewhat simpler way than has been found before. In rubber, the main idea is that the oscillations of cracks follow from basic features of fracture mechanics and are independent of details of the crack equation of motion. From the fact that oscillations exist, one can deduce some conditions on forms that equations of motion can take.

This present study is focused on the onset of oscillations in gels and rubber. It is interesting to investigate the relation between wavelength of oscillations and initial loading, and this will be left for future work.

5.3 Discrete Model of Hydraulic Fracture

Hydraulic fracturing is a stimulation treatment wherein highly-pressurized fluids are injected into reservoirs to generate fractures there. Classical theoretical models of hydraulic fracturing were developed based on an assumption of a single planar hydraulic fracture; however, this widely-held assumption was challenged by recent studies. More and more evidence suggests that hydraulic fractures can be complex, but the physical mechanisms responsible for the formation of complex fracture networks are still poorly understood.

This study developed a lattice-based model to investigate the complexity of fracture networks. The basic ingredients of this model are two-dimensional linear elasticity, fracture mechanics, fluid flow. This model provides three major advantages: it can accommodate arbitrary geometries, it can reasonably resolve kilometer-scale wells, and it adds the features of anisotropy

and heterogeneity without difficulty.

This model has been validated via a comparison with the KGD model. In a multi-fracture interference study, a series of pilot simulations was systematically tested for complex geometries under realistic operation conditions, including flexible boundary conditions, randomness in elastic properties and perforations. Complex fracture networks were observed in a perforated medium in this study. In general, the more initial seed cracks were inserted, the more complex fracture networks were observed in the study; the results also show that the exterior seed cracks grew much faster than the interior ones.

In conclusion, these pilot results demonstrate the present model's ability to simulate hydraulic fracturing under a variety of operation conditions. The main results of a multi-fracture interference study show that perforation is likely to increase the complexity of fracture networks. In addition, the competition between neighboring fractures plays an important role in fracture network formation.

Due to the high computational demand, all the tests in this study were limited to pseudo-3D simulations on the scales of tens of meters in length. A parallel version of the simulation code will be needed to run efficiently on parallel computers to reach the reservoir scale simulations. In future work, we will investigate the relation between perforation angles and complexity of fracture networks. In addition, a qualitative analysis of the fracture complexity would be of great interest for future research.

Appendices

Appendix A

Length scale limit

Consider a semi-infinite perfectly straight crack running to the right along the x-axis at speed v in an infinite strip, as shown in fig. 3.4. The strip is stretched to a desired extension state (λ_x, λ_y), where λ_x and λ_y are the extension ratios along the x direction and the y direction, respectively. The original height of the strip is H. The sample height under deformed is $H' = \lambda_y H$. Let Σ_{xx} and Σ_{yy} represent the stresses far to the right along the x direction and the y direction, respectively.

The non-zero stress intensity factor for this crack is [18]

$$K_I^0 = \Sigma_{yy}\sqrt{H}\sqrt{\frac{\mu c_s^2 R}{Y v^2 \alpha_d}}. \tag{A.1}$$

Here μ is the shear modulus, Y is Young's modulus, $\alpha_d = \sqrt{1 - v^2/c_d^2}$, $R = 4\alpha_d\alpha_s - (1 + \alpha_s^2)^2$, c_s and c_d are the shear wave speed and the dilatational wave speed, respectively.

For a slightly curved crack in a linear elastic material, Cotterell and Rice [11] found expressions for the coefficients of the stress field accurate to

first order in η. They are

$$K_I(x) = K_I^0, \tag{A.2}$$

and

$$K_{II}(x) = \frac{\theta(x)}{2} K_I^0 - T\sqrt{\frac{\pi}{2}} \int_{-\infty}^{x} \frac{\theta(\xi)}{\sqrt{x-\xi}} d\xi. \tag{A.3}$$

Consider a linear mode $\eta_q(x) = \eta_0 e^{qx}$, where $\eta_0 \ll H$. Equation (A.3) for this mode can be rewritten as

$$K_{II}(x) = K_I^0 \left(\frac{1}{2} - \frac{T}{K_I^0} \sqrt{\frac{2}{q}} \right) \theta_q(x). \tag{A.4}$$

Let Λ represent the wavelength of oscillating cracks. Thus, $|q| \sim 2\pi/\Lambda$ at oscillations. The T-stress is $T = \Sigma_{xx} - \Sigma_{yy}$ [11, 14].

From eq. (A.1), at oscillations, we have

$$\frac{T}{K_I^0}\sqrt{\frac{1}{q}} \sim \left(\frac{\Sigma_{xx} - \Sigma_{yy}}{\Sigma_{yy}} \right) \sqrt{\frac{Y v^2 \alpha_d(v)}{\mu c_s^2 R(v)}} \sqrt{\frac{\Lambda}{H}} \to 0 \quad \text{if } \Lambda/H \to 0. \tag{A.5}$$

Thus, when $\Lambda \ll H$, the second term on the right hand side in eq. (A.4) is negligible.

Appendix B

Energy release rate

The energy release rate, G, is the the total strain potential energy released per unit of area of crack extension, and it can be calculated by using the following integral:

$$G = \int_{\Gamma} \left[(U + E_k)\, n_x - \sigma_{ji} n_j \frac{\partial u_i}{\partial x} \right] d\Gamma, \tag{B.1}$$

Here i and j range over x and y. n_i is the i component of the normal unit vector of Γ. U is strain energy density. The kinetic energy is described by $E_{\mathrm{k}} = \frac{\rho}{2}\left(\dot{u}_x^2 + \dot{u}_y^2\right)$ [18, 55].

B.1 Two extreme cases

Let's consider two extreme cases: $\Gamma \to 0$ and $\Gamma \to \infty$.

B.1.1 In the case of $\Gamma \to 0$

For mode I crack, the near-tip stress fields (outside of the fracture process zone) in polar coordinates (r, ϕ) with the origin at the crack tip can

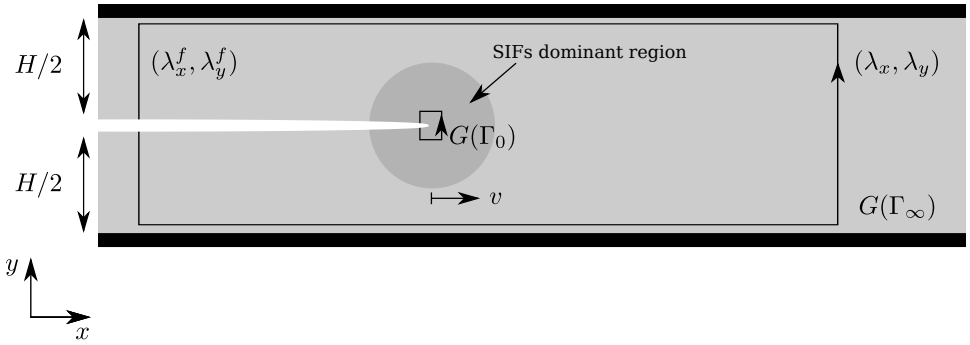

Figure B.1: Sketch shows two contour paths, Γ_0 and Γ_∞, for the energy release rate integral shown in eq. (B.1).

be expanded as a series [11, 18, 62]

$$\sigma_{ij}(r,\phi) \sim \frac{K_I}{\sqrt{2\pi r}} f_{ij}^I(v,\phi) + T\delta_{ix}\delta_{jx} + O\left(\sqrt{r}\right), \tag{B.2}$$

where i and j range over x and y. In eq. (B.2), the first term of the near-tip stress fields associated with the stress intensity factor K_I is singular and $f_{ij}^I(v,\phi)$ is a known universal function [8, 18]; T represents the T-stress, a non-singular local stress parallel to the crack.

From eq (B.4), eq. (B.1) and (B.2), the energy release rate for mode I crack in the Neo-Hookean model is

$$G(\Gamma_0) = \frac{K_I^2}{2\mu\alpha_s}, \tag{B.3}$$

where $\alpha_s = \sqrt{1-(v/c_s)^2}$.

B.1.2 In the case of $\Gamma \to \infty$

On the other hand, as $\Gamma \to \infty$, the contributions to the energy release rate are from the segments of Γ_∞ parallel to y-axis at $x \to \pm\infty$.

We assume that rubber is Neo-Hookean, so that the energy of a uniform sample in biaxial strain is (up to an additive constant U_0) [39, 40, 42]

$$U = \frac{\mu}{2}\left[\lambda_x^2 + \lambda_y^2 + 1/\left(\lambda_x^2\lambda_y^2\right)\right] + U_0. \tag{B.4}$$

Here $\vec{u}\,(\vec{r})$ is the distance between the origin and a mass point that was originally at $\vec{r}$, and μ is the shear modulus.

The experiments we discuss take place for extensions on the order of 2 or more [13], allowing us to neglect the final term in eq. (3.15) except in the wake of the crack where the rubber has relaxed to a state described by $\lambda_x^r = \lambda_x$ and $\lambda_y^r = 1/\sqrt{\lambda_x}$, which minimizes the energy in λ_y when λ_x is held constant.

The elastic energy per unit length for a strip of height H is

$$w(\lambda_x, \lambda_y, H) = \int_{-\frac{H}{2}}^{\frac{H}{2}} U(\lambda_x, \lambda_y) dy. \tag{B.5}$$

The dynamic energy release rate is

$$G\left(\Gamma_\infty\right) = w(\lambda_x, \lambda_y, H) - w(\lambda_x^r, \lambda_y^r, H). \tag{B.6}$$

Plug Equation (B.5) into eq. (B.6) to have

$$G\left(\Gamma_{\infty}\right) = \frac{\mu}{2} H\left(\lambda_y^2 - 2/\lambda_x\right). \tag{B.7}$$

B.1.3 Energy balance

For a crack moving in an elastic material under steady equilibrium conditions, the amount of energy released from the body is equal to the amount of energy flowing to the crack tip, i.e., $G\left(\Gamma_0\right) = G\left(\Gamma_{\infty}\right)$. For a mode I crack, this energy balance condition leads to

$$K_I = \sqrt{2\mu\alpha_s G\left(\Gamma_{\infty}\right)} = \mu\sqrt{\alpha_s H\left(\lambda_y^2 - 2/\lambda_x\right)}. \tag{B.8}$$

Appendix C

Perturbation analysis

Slightly curved or kinked cracks in the linear elastic material have been studied by Cotterell and Rice [11]. Here, we apply their analysis to crack propagation in rubber sheets under great deformation. The analysis begins with a problem of a finite quasi-static crack which is slightly curved in an infinite medium. Then, we extend the results to an semi-infinite crack problem.

Figure C.1 shows a slightly curved crack and a reference perfectly straight crack. Let $L_0^{\pm}$ denote the crack surface for a perfect straight crack with two ends, $-b$ and a, along the x-axis, where plus and minus signs represent the upper surface and lower surface, respectively. Let $L^{\pm}$ represent the crack surface for a slightly curved crack. Suppose the crack is opened by the normal and shear tractions T_n and T_s on the crack surfaces. For a crack grows under uniform stresses, conventional superposition methods can be used to satisfy the free traction boundary conditions on the crack surfaces. The stress intensity factors K_I and K_{II} for these two problems are identical.

C.1 Boundary conditions

The equations of motions for u_x and u_y can be completely decoupled as $\ddot{u}_x = c_s^2 \nabla^2 u_x$ and $\ddot{u}_y = c_s^2 \nabla^2 u_y$ based on eq. (B.4) [39, 40]. Without body force, the equations of motion become Laplace's equations and u_x and u_y are two harmonic functions [39, 40].

Given $z = x+iy$. The strain fields around the crack tip can be described as $u_x = f(z) + \overline{f(z)}$ and $u_y = g(z) + \overline{g(z)}$, where $f(z)$ and $g(z)$ are two analytic functions. Let $\phi(z) = i\mu f'(z)$ and $\psi(z) = i\mu g'(z)$ and define $A(z) \equiv \psi(z) - i\phi(z)$ and $B(\overline{z}) \equiv \overline{\psi(z)} - i\overline{\phi(z)}$. Because u_x and u_y are completely decoupled, the stress fields can be written as

$$\sigma_{xx} = \mu \frac{\partial u_x}{\partial x} = \mu \left[f'(z) + \overline{f'(z)} \right] = -i \left[\phi(z) - \overline{\phi(z)} \right],$$

$$\sigma_{xy} = \mu \frac{\partial u_x}{\partial y} = i\mu \left[f'(z) - \overline{f'(z)} \right] = \left[\phi(z) + \overline{\phi(z)} \right],$$

$$\sigma_{yx} = \mu \frac{\partial u_y}{\partial x} = \mu \left[g'(z) + \overline{g'(z)} \right] = -i \left[\psi(z) - \overline{\psi(z)} \right],$$

$$\sigma_{yy} = \mu \frac{\partial u_y}{\partial y} = i\mu \left[g'(z) - \overline{g'(z)} \right] = \left[\psi(z) + \overline{\psi(z)} \right].$$

Some useful combinations of stress fields may be expressed in terms of $A(z)$ and $B(\overline{z})$ as follows,

$$\sigma_{yy} - i\sigma_{xy} = A(z) + B(\overline{z}), \tag{C.1}$$

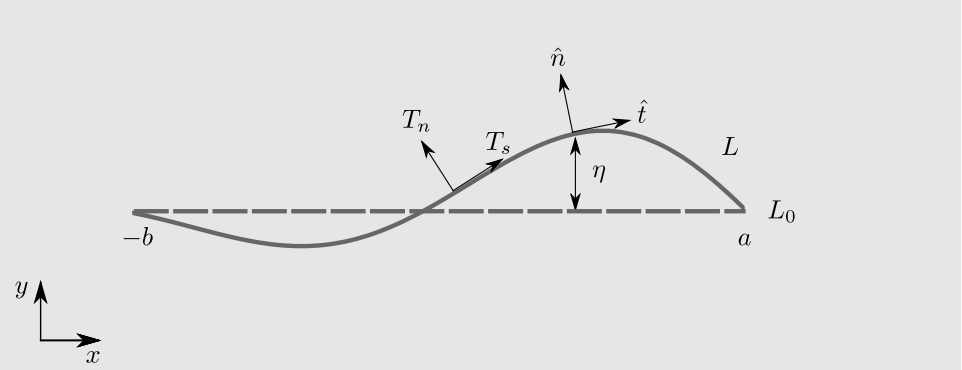

Figure C.1: Sketch shows a close view of a curved crack (in solid line) in an infinite medium. The crack is opened by the normal and shear tractions T_n and T_s on the crack surfaces and the stresses at infinity are zero. A reference perfectly straight crack (in dashed line) has two ends, $-b$ and a. The deviation of the actual crack path from the straight line is denoted by η. $\hat{n}$ and $\hat{t}$ are normal unit vector and tangential unit vector to the crack path.

and

$$\sigma_{xx} + i\sigma_{yx} \quad = \quad A(z) - B(\overline{z}). \tag{C.2}$$

Let $\eta(x)$ represent the deviation of the perturbed crack surface from straightness. Let $\hat{n}$ and $\hat{t}$ represent the unit vectors normal and tangential to the crack surfaces, respectively (fig. C.1). Then $\hat{n} = (n_x, n_y) = (-\sin\eta'(x), \cos\eta'(x))$ and $\hat{t} = (t_x, t_y) = (n_y, -n_x)$. Let θ describe the tangent angle of crack measured from the x-axis, and $\theta(x) \approx \partial\eta/\partial x$ when the η is much smaller than crack size.

Assume the crack is opened by the normal and shear surface tractions T_n and T_s, and let f_n and f_s represent the normal and shear restoring forces

due to the deformations on the crack surfaces, respectively. In quasi-static equilibrium, we have $(T_n - iT_s) + (f_n - if_s) = 0$.

The x and y components of the restoring force $\vec{f}$ on the crack surfaces are given by

$$\begin{pmatrix} f_x \\ f_y \end{pmatrix} = \begin{pmatrix} \sigma_{xx} & \sigma_{xy} \\ \sigma_{yx} & \sigma_{yy} \end{pmatrix} \begin{pmatrix} n_x \\ n_y \end{pmatrix}.$$

Then, we have

$$\begin{pmatrix} f_n \\ f_s \end{pmatrix} = \begin{pmatrix} n_x & n_y \\ t_x & t_y \end{pmatrix} \begin{pmatrix} f_x \\ f_y \end{pmatrix} = \begin{pmatrix} n_x & n_y \\ n_y & -n_x \end{pmatrix} \begin{pmatrix} f_x \\ f_y \end{pmatrix}. \tag{C.3}$$

From eq. (C.1), eq. (C.2) and eq. (C.3), the boundary condition is

$$\begin{aligned} (f_n - if_s)(z) &= A(z) + e^{-2i\theta} B(\overline{z}) \\ &= A(z) + B(\overline{z}) - 2i\eta' B(\overline{z}) + O\left(\eta^2\right). \end{aligned} \tag{C.4}$$

We introduce two functions $F(z)$ and $W(z)$, which are associated with $A(z)$ and $B(z)$. Both $F(z)$ and $W(z)$ are analytic everywhere except on the straight cut, L_0. $F^{\pm}$ and $W^{\pm}$ represent the boundary values on the upper and lower surfaces of L_0.

Expand F and W to the first order,

$$F(z) = F_0(z) + F_1(z) + O\left(\eta^2\right),$$

and

$$W(z) = W_0(z) + W_1(z) + O\left(\eta^2\right),$$

where the subscripts denoted by 0 and 1 refer to the zeroth and the first order solutions, respectively.

At the point $z_L = x + i\eta$ on $L^{\pm}$, we may express $A(z_L)$ and $B(\overline{z_L})$ in terms of F and W:

$$A^{\pm}(z_L) = F_0^{\pm}(x) + \left[F_1^{\pm} + i\eta\left(F_0^{\pm}\right)'\right](x), \tag{C.5}$$

and

$$B^{\mp}(\overline{z_L}) = W_0^{\mp}(x) + \left[W_1^{\mp} - i\eta\left(W_0^{\mp}\right)'\right](x). \tag{C.6}$$

From eq. (C.4), eq. (C.5) and eq. (C.6), the boundary condition becomes

$$(f_n - if_s)(z_L) = E_0^{\pm}(x) + E_1^{\pm}(x), \tag{C.7}$$

where

$$E_0^{\pm}(x) \equiv \left(F_0^{\pm} + W_0^{\mp}\right)(x), \tag{C.8}$$

$$E_1^{\pm}(x) \equiv \left(F_1^{\pm} + W_1^{\mp}\right)(x) + i\eta\left(F_0^{\pm} - W_0^{\mp}\right)'(x) - 2i\eta' W_0^{\mp}(x). \tag{C.9}$$

C.2 Useful integrals, I and J

Here we define two useful integrals, I and J, for the following analysis

$$I(T,z) \equiv \frac{1}{\pi\sqrt{(z-a)(z+b)}}\int_{-b}^{a} T\frac{\sqrt{(a-x)(b+x)}}{z-x}dx,$$

and

$$J(T) \equiv \sqrt{\frac{2}{\pi(a+b)}} \int_{-b}^{a} T \sqrt{\frac{b+x}{a-x}} dx.$$

Two useful relationships between I and J are listed here:

$$\lim_{r \to 0} \sqrt{2\pi r} I(T, a+r) = J(T),$$

and

$$\lim_{r \to 0} \sqrt{2\pi r} r I'(T, a+r) = -\frac{1}{2} J(T).$$

C.3 Perturbation analysis

For a slightly curved crack, we know that the leading term of T_n is $O(\eta^0)$ and the leading term of T_s is $O(\eta^1)$. Express eq. (C.7) in the zeroth order term and the first order term separately,

$$O\left(\eta^0\right): \qquad E_0^{\pm}(x) = f_n = -T_n, \tag{C.10}$$

$$O\left(\eta^1\right): \qquad E_1^{\pm}(x) = -i f_s = i T_s. \tag{C.11}$$

Let's define $T_0 = T_n$ and $T_1 = -i(T_s - \eta' T_n)$.

C.3.1 The zeroth order solutions

From eq. (C.8) and eq. (C.10), the boundary values of $F_0(z) + W_0(z)$ and $F_0(z) - W_0(z)$ are given by

$$(F_0 + W_0)^+ + (F_0 + W_0)^- = -2T_0,$$

and

$$(F_0 - W_0)^+ - (F_0 - W_0)^- = 0.$$

Based on Mushkelishvili's approach [8, 11, 44, 57] and the Plemelj formula [57], we obtain

$$F_0(z) = W_0(z) = \frac{1}{2} I(T_0, z). \tag{C.12}$$

On $L_0^{\pm}$, we have

$$F_0^+(x) = F_0^-(x). \tag{C.13}$$

C.3.2 The first order solutions

Plug the zeroth order solutions to eq. (C.11) to obtain the boundary values of $F_1(z) + W_1(z)$ and $F_1(z) - W_1(z)$, and they are

$$(F_1 + W_1)^+ + (F_1 + W_1)^- = -2T_1,$$

and

$$(F_1 - W_1)^+ - (F_1 - W_1)^- = 0.$$

Therefore, we have

$$F_1(z) = W_1(z) = \frac{1}{2} I(T_1, z). \tag{C.14}$$

Consider a point z_c very close to the crack tip z_{tip} at $x = a$. Given $z_c = x_c + i\omega r$, where $\omega = \eta'(a)$ represents the slope of the the crack tip at $x = a$ and $r \ll a$. The distance between z_c and the crack tip z_{tip} is $|z_c - z_{\text{tip}}| = \sqrt{r}\,(1+\omega^2)^{1/4} \approx \sqrt{r} + O(\eta^2)$. Let $\sigma_{\omega\omega}$ and $\sigma_{r\omega}$ represent the normal and shear stress at z_c.

From eq. (C.7), eq. (C.12) and eq. (C.14), we obtain

$$\begin{aligned}
\sqrt{2\pi r}\,(\sigma_{\omega\omega} - i\sigma_{r\omega})\Big|_{x_c + i\omega r} &= \sqrt{2\pi r}\,(F_0 + W_0 + F_1 + W_1)(x_c) \\
&\quad + \sqrt{2\pi r}\left[i\eta\,(F_0 - W_0)'\right](x_c) \\
&\quad + \sqrt{2\pi r}\,(-2i\eta' W_0)(x_c).
\end{aligned} \tag{C.15}$$

Let $r \to 0$, and eq. (C.15) becomes

$$\begin{aligned}
\lim_{r\to 0} \sqrt{2\pi r}\,(\sigma_{\omega\omega} - i\sigma_{r\omega})\Big|_{x_c + i\omega r} &= J(T_0 + T_1 - i\omega T_0) \\
&= J(T_n) - iJ(T_s - \eta' T_n + \omega T_n).
\end{aligned} \tag{C.16}$$

Based on the definition of stress intensity factors, the left hand side of eq. (C.16) is $K_I - iK_{II}$. Let $q_I = T_n$ and $q_{II} = T_s - \eta' T_n + \omega T_n$. Then, the stress intensity factors for a slightly curved crack can be found by the following equation

$$K_I - iK_{II} = J\left(q_I\right) - iJ\left(q_{II}\right). \tag{C.17}$$

For a straight crack, i.e., $\eta = \omega = 0$, the nonzero stress intensity factors is

$$K_I = \sqrt{\frac{\pi\left(a+b\right)}{2}}\Sigma_{yy}.$$

C.3.3 Superposition approaches

Here we can find the first order solution of the tractions T_n and T_s by using the conventional superposition method [8, 18]. Assume the straight crack is opened by the uniform biaxial stresses Σ_{xx} and Σ_{yy}, and then the normal and shear traction based on the perturbation approach are given by

$$T_n = \Sigma_{yy} + \eta'^2\left(\Sigma_{xx} - \Sigma_{yy}\right), \tag{C.18}$$

and

$$T_s = -\eta'\left(\Sigma_{xx} - \Sigma_{yy}\right). \tag{C.19}$$

Plug eq. (C.18) and eq. (C.19) to eq. (C.17), we obtain

$$K_I = K_I^0,$$

and

$$K_{II} \;=\; \omega K_I^0 - J\left(\eta' \Sigma_{xx}\right). \tag{C.20}$$

Here $K_I^0 = \sqrt{\frac{\pi(a+b)}{2}}\Sigma_{yy}$, the nonzero stress intensity factor for a straight crack.

C.3.4 Semi-infinite crack problem

Here, we extend our analysis to a semi-infinite crack problem. Let $b \to \infty$ and we have

$$\begin{aligned}
\lim_{b\to\infty} J\left(\eta' \Sigma_{xx}\right) &= \lim_{b\to\infty} \sqrt{\frac{2}{\pi\left(a+b\right)}} \int_{-b}^{a} \Sigma_{xx} \eta'\left(x\right) \sqrt{\frac{b+x}{a-x}} dx \\
&\approx \Sigma_{xx} \sqrt{\frac{2}{\pi}} \int_{-\infty}^{a} \eta'\left(x\right) \sqrt{\frac{1}{a-x}} dx.
\end{aligned}$$

Hence, eq. (C.20) becomes

$$K_{II}\left(a\right) \;=\; K_I^0 \eta'\left(a\right) - \Sigma_{xx} \sqrt{\frac{\pi}{2}} \int_{-\infty}^{a} \frac{\eta'\left(\xi\right)}{\sqrt{x-\xi}} d\xi. \tag{C.21}$$

Bibliography

[1] J. Adachi, E. Siebrits, A. Peirce, and J. Desroches. Computer simulation of hydraulic fractures. *International Journal of Rock Mechanics and Mining Sciences*, 44(5):739–757, July 2007.

[2] M. Adda-Bedia, M. Arias, M. B. Amar, and F. Lund. Generalized Griffith criterion for dynamical fracture and the stability of crack motion at high velocities. *Physical Review E*, 60:2366–2376, 1999.

[3] E. Bouchbinder. Dynamic crack tip equation of motion: high-speed oscillatory instability. *Physical review letters*, 103(16):164301, 2009.

[4] E. Bouchbinder, J. Fineberg, and M. Marder. Dynamics of simple cracks. *Annual Review of Condensed Matter Physics, Vol 1*, 1:371–395, 2010.

[5] E. Bouchbinder, A. Livne, and J. Fineberg. Weakly nonlinear theory of dynamic fracture. *Physical Review Letters*, 101:264302, 2008.

[6] E. Bouchbinder, A. Livne, and J. Fineberg. The 1/r singularity in weakly nonlinear fracture mechanics. *Journal of the Mechanics and Physics of Solids*, 57:1568–1577, 2009.

[7] M. C. Boyce and E. M. Arruda. Constitutive models of rubber elasticity: A review. *Rubber Chemistry and Technology*, 73(3):504–523, July 2000.

[8] K. B. Broberg. *Cracks and Fracture*. Academic Press, San Diego, 1999.

[9] C. H. Chen, H. P. Zhang, J. Niemczura, K. Ravi-Chandar, and M. Marder. Scaling of crack propagation in rubber sheets. *EPL (Europhysics Letters)*, 96(3):36009, 2011.

[10] H. Cooley and D. K. Hydraulic fracturing and water resources: Separating the frack from the fiction. Oakland, California, 2012. Pacific Institute.

[11] B. Cotterell and J. R. Rice. Slightly curved or kinked cracks. *International Journal of Fracture*, 16:155, 1980.

[12] J. L. Daniels, G. A. Waters, J. H. L. Calvez, D. Bentley, and J. T. Lassek. Contacting more of the barnett shale through an integration of real-time microseismic monitoring, petrophysics, and hydraulic fracture design. In *SPE Annual Technical Conference and Exhibition*, Anaheim, California, U.S.A., 2007. Society of Petroleum Engineers.

[13] R. D. Deegan, P. Petersan, M. Marder, and H. L. Swinney. Oscillating fracture paths in rubber. *Physical Review Letters*, 88:14304, 2002.

[14] T. Fett. *Stress Intensity Factors, T-stresses, Weight Functions: Supplement Volume*. Vol. 55. KIT Scientific Publishing, 2009.

[15] J. Fineberg, S. Gross, M. Marder, and H. Swinney. Instability in dynamic fracture. *Physical Review Letters*, 67:457–460, 1991.

[16] J. Fineberg and M. Marder. Instability in dynamic fracture. *Physics Reports*, 313:1–108, 1999.

[17] M. Fisher, C. Wright, B. Davidson, A. Goodwin, E. Fielder, W. Buckler, and N. Steinsberger. Integrating fracture mapping technologies to optimize stimulations in the barnett shale. In *SPE Annual Technical Conference and Exhibition*, San Antonio, Texas, 2002. Society of Petroleum Engineers.

[18] L. B. Freund. *Dynamic Fracture Mechanics*. Cambridge University Press, Cambridge, 1990.

[19] H. Gao. Surface roughening and branching instabilities in dynamic fracture. *Journal of the Mechanics and Physics of Solids*, 41:457–486, 1993.

[20] J. Geertsma and F. D. Klerk. A rapid method of predicting width and extent of hydraulically induced fractures. *Journal of Petroleum Technology*, 21(DEC):1571–&, 1969.

[21] P. Geiser, A. Lacazette, and J. Vermilyes. Beyond 'dots in a box': an empirical view of reservoir permeability with tomographic fracture imaging. *EAGE First Break*, 30(5):63–69, July 2012.

[22] H. Gercek. Poisson's ratio values for rocks. *International Journal of Rock Mechanics and Mining Sciences*, 44(1):1–13, Jan. 2007.

[23] J. L. Gidley and S. of Petroleum Engineers (U.S.). *Recent Advances in Hydraulic Fracturing*. Henry L. Doherty Memorial Fund of AIME, Society of Petroleum Engineers, 1989.

[24] T. Goldman, A. Livne, and J. Fineberg. Acquisition of inertia by a moving crack. *Phys. Rev. Lett.*, 104:114301, Mar 2010.

[25] R. V. Goldstein and R. Salganik. Brittle fracture of solids with arbitrary cracks. *International Journal of Fracture*, 10:507–523, 1974.

[26] A. A. Griffith. The phenomena of rupture and flow in solids. *Philosophical Transactions of the Royal Society of London. Series A, Containing Papers of a Mathematical or Physical Character*, 221(582-593):163–198, 1921.

[27] J. A. Hodgdon and J. P. Sethna. Derivation of a general three-dimensional crack-propagation law: A generalization of the principle of local symmetry. *Physical Review B*, 47(9):4831, 1993.

[28] R. W. Howarth, A. Ingraffea, and T. Engelder. Natural gas: Should fracking stop? *Nature*, 477(7364):271–275, Sept. 2011.

[29] J. D. Hughes. Energy: A reality check on the shale revolution. *Nature*, 494(7437):307–308, Feb. 2013.

[30] G. R. Irwin. Fracture dynamics. In *Fracturing of metals*, pages 147–166, Cleveland, 1948. American Society for Metals.

[31] G. R. Irwin. Analysis of stresses and strains near the end of a crack traversing a plate. *Journal of Applied Mechanics*, 24:361–364, 1957.

[32] B. L. Karihaloo, L. M. Keer, S. Nemat-Nasser, and A. Oranratnachai. Approximate description of crack kinking and curving. *Journal of Applied Mechanics*, 48(3):515–519, Sept. 1981.

[33] S. A. Khristianovic and Y. P. Zheltov. Formation of vertical fractures by means of highly viscous liquid. In *SPE Annual Technical Conference and Exhibition*, pages 579–586, Rome, 1955. Proceedings of the fourth world petroleum congress.

[34] G. J. Lake, C. C. Lawrence, and A. G. Thomas. High-speed fracture of elastomers: Part i. *Rubber Chemistry and Technology*, 73(5):801–817, 2000.

[35] A. Livne, O. Ben-David, and J. Fineberg. Oscillations in rapid fracture. *Physical Review Letters*, 98:124301, 2007.

[36] A. Livne, E. Bouchbinder, and J. Fineberg. The breakdown of linear elastic fracture mechanics near the tip of a rapid crack. *Physical Review Letters*, 101:264301, 2008.

[37] M. Marder. New dynamical equation for cracks. *Physical Review Letters*, 66:2484–2487, 1991.

[38] M. Marder. Effect of atoms on brittle fracture. *International Journal of Fracture*, 130:517–555, 2004.

[39] M. Marder. Shock-wave theory of rupture of rubber. *Physical Review Letters*, 94:048001, 2005.

[40] M. Marder. Supersonic rupture of rubber. *Journal of the Mechanics and Physics of Solids*, 54:491–532, 2006.

[41] M. Marder and S. Gross. Origin of crack tip instabilities. *Journal of the Mechanics and Physics of Solids*, 43:1–48, 1995.

[42] M. Mooney. A theory of large elastic deformation. *Journal of Applied Physics*, 11:582–92, 1940.

[43] P. H. Mott, C. M. Roland, and R. D. Corsaro. Acoustic and dynamic mechanical properties of a polyurethane rubber. *Journal of the Acoustical Society of America*, 111(4):1782–1790, Apr. 2002.

[44] N. I. Muskhelishvili. *Some Basic Problems in the Mathematical Theory of Elasticity*. Noordhoff, Groningen, 1952.

[45] J. Niemczura. *On the response of rubbers at high strain rates*. PhD thesis, The University of Texas at Austin, 2009.

[46] J. Niemczura and K. Ravi-Chandar. On hysteretic response and stationary phase fronts in rubber. *Continuum Mechanics and Thermodynamics*, 22:469–484, 2010.

[47] J. Niemczura and K. Ravi-Chandar. On the response of rubbers at high strain rates–III. effect of hysteresis. *Journal of the Mechanics and Physics of Solids*, 59(2):457–472, 2011.

[48] R. P. Nordgren. Propagation of a vertical hydraulic fracture. *Society of Petroleum Engineers Journal*, 12(4):306–314, 1972.

[49] G. E. Oleaga. Remarks on a basic law for dynamic crack propagation. *Journal of the Mechanics and Physics of Solids*, 49:2273–2306, 2001.

[50] J. E. Olson. Multi-fracture propagation modeling: Applications to hydraulic fracturing in shales and tight gas sands. In *The 42nd U.S. Rock Mechanics Symposium (USRMS)*, San Francisco, California, 2008. American Rock Mechanics Association.

[51] E. Orowan. Energy criteria of fracture. *Weld. Res. Supp.*, 34:157, 1955.

[52] T. K. Perkins and L. R. Kern. Widths of hydraulic fractures. *Transactions of the Society of Petroleum Engineers of Aime*, 222(9):937–949, 1961.

[53] P. J. Petersan, R. D. Deegan, M. Marder, and H. L. Swinney. Cracks in rubber under tension exceed the shear wave speed. *Physical Review Letters*, 93:015504/1–4, 2004.

[54] K. Ravi–Chandar and W. G. Knauss. An experimental investigation into dynamic fracture:III. On steady-state crack propagation and crack branching. *International Journal of Fracture*, 26:141–154, 1984.

[55] K. Ravi-Chandar. *Dynamic Fracture*. Elsevier, Amsterdam, 2004.

[56] O. Reynolds. On the theory of lubrication and its application to mr. beauchamp tower's experiments, including an experimental determination of the viscosity of olive oil. *Philosophical Transactions of the Royal Society of London*, 177:157–234, Jan. 1886.

[57] J. R. Rice. Mathematical analysis in the mechanics of fracture. *Fracture: An Advanced Treatise*, 2:191–311, 1968.

[58] S. A. Shapiro, C. Dinske, and E. Rothert. Hydraulic-fracturing controlled dynamics of microseismic clouds. *Geophys. Res. Lett.*, 33(14):L14312, 2006.

[59] L. Slepyan. Dynamics of a crack in a lattice. *Soviet Physics Doklady*, 26:538–540, 1981.

[60] I. N. Sneddon. The distribution of stress in the neighbourhood of a crack in an elastic solid. *Proceedings of the Royal Society of London. Series A. Mathematical and Physical Sciences*, 187(1009):229–260, 1946.

[61] H. Van Eekelen. Hydraulic fracture geometry: Fracture containment in layered formations. *Society of Petroleum Engineers Journal*, 22(3):341–349, 1982.

[62] M. Williams. On the stress distribution at the base of a stationary crack. *Journal of Applied Mechanics*, 24:109–114, 1957.

[63] H. P. Zhang, J. Niemczura, G. Dennis, K. Ravi-Chandar, and M. Marder. Toughening effect of strain-induced crystallites in natural rubber. *Physical Review Letters*, 102(24):245503, 2009.